



UNIVERSITÀ DEGLI STUDI DI FERRARA

Tesi di laurea in Fisica

**Simulations and experimental activity in
support of the ASTENA concept mission
proposed to ESA**

Relatore:

Prof. Piero Rosati

II Relatore:

Dott. Enrico Virgilli

Laureanda:

Lisa Ferro

Anno Accademico 2020/2021

Contents

Introduction	1
1 The ASTENA concept mission	5
1.1 Open cases in high energy astrophysics	5
1.1.1 The positron line puzzle: 511 keV annihilation emission from the Galactic Centre	5
1.1.2 Physics of Type-Ia and core-collapse supernovae	7
1.1.3 Prompt emission and afterglows of GRBs	8
1.1.4 Low Luminosity GRBs and other fast transients	10
1.2 The ASTENA payload	12
1.2.1 Wide Field Monitor-Imaging Spectrometer (WFM-IS)	12
1.2.2 Narrow Field Telescope (NFT)	13
2 Efficiency of Si and Ge crystals	17
2.1 Bragg's Law of Diffraction and Laue Lenses	17
2.1.1 Diffraction in Perfect Crystals	21
2.1.2 Malgrange Theory for perfect curved crystals	25
2.2 Modelling a crystal	26
2.2.1 Diffraction by higher order planes	33
2.2.2 Estimated efficiency for the Ge(111) and Si(111) crystals	34
3 Simulations for the NFT	37
3.1 The "Laue Lens Library" simulation code	37
3.2 GUI programming in Python	39
3.2.1 The <i>Tkinter</i> library	40
3.3 The new GUI	41
3.3.1 "General Options" panel	42
3.3.2 "Lens Configuration" panel	42
3.3.3 "Crystals' Parameters" panel	43
3.3.4 "Lens Parameters" panel	43
3.3.5 "Source Parameters" and "Detector Parameters" panels	44
3.4 Simulations of the NFT detector	45
3.4.1 The MEGAlib software	45

3.4.2	Detector geometry	46
3.4.3	Detector performances estimation	47
3.4.4	Detector spectral response	49
4	Double Laue diffraction	55
4.1	Grazing incidence reflection and Kirkpatrick-Baez mirrors .	55
4.2	Double Bragg's Diffraction in Laue configuration	58
4.2.1	Experimental set-up and verification	65
4.2.2	Prospects for hard X-ray imaging with reduced off-axis aberrations	70
	Conclusions	71

List of Figures

1.1	Map of the 511 keV emission line measured by INTEGRAL/SPI (Weidenspointner et al. 2008). The emission show a symmetric central bulge and a clearly asymmetric diffuse disk. . . .	6
1.2	The expected gamma ray spectrum for a Ia SN at 20 days of the explosion, according to different models for the explosion mechanism. Reprinted from Gómez-Gomar et al. (1998)	7
1.3	Afterglow data measured by Swift/XRT and Fermi/LAT. ASTENA will cover the region highlighted in yellow. (Reprinted from Guidorzi et al. (2019), adapted from Ajello et al. (2018)	9
1.4	Artistic view of the ASTENA Spacecraft. Reprinted from Frontera et al. 2019	12
1.5	<i>Left:</i> Schematization of a single detection unit of the WFM-IS. The whole instrument is composed by 12 detection units. <i>Right:</i> Schematization of one of the module composing the detection units of WFM-IS. Each unit is an array of 4 x 8 modules.	13
1.6	Minimum detectable polarization at 3σ for the WFM-IS. The MDP is evaluated for a GRB with a duration of 20 s and two different value of fluence. The assumed spectrum of the GRB is a Band law with typical values $\alpha = 1.0$, $\beta = 2.3$ and peak energy of 300 keV.	14
1.7	ASTENA/NFT continuum sensitivity compared to other past or current missions for an observation time of 10^5 s.	15
1.8	Estimated line sensitivity for ASTENA/NFT for an observation time of 10^5 s.	15
2.1	Schematic picture of X-ray diffraction in a crystal with interplanar spacing equal to d_{hkl} . Diffraction consist in an interaction between the photon and the periodic lattice structure of the crystal. The result of this interaction is that the incoming beam appears to have been deviated by the crystal to a new direction associated to the angle θ_B	18

2.2	Schematic picture of a crystal in Bragg geometry (left) and Laue geometry (right).	19
2.3	Schematic representation of a Laue lens. The Lens is a spherical cap with rings of crystals fixed above. All the crystals are oriented in such a way that the diffracted radiation is focused in the same point. The innermost ring with radius r_{min} diffracts higher energies, while the one with radius r_{max} reacts to the lower energies.	20
2.4	Image of a parallel beam generated by a flat crystal. The beam is redirected, but not focused. The resulting image has a size comparable with the size of the crystal tile.	22
2.5	Representation of a perfect curved crystal. The crystal has a primary curvature radius R_p and the diffracting planes themselves show a secondary curvature radius R_s , which determines an angular spread of the planes Ω	23
2.6	<i>Left:</i> Image of a parallel beam generated by a curved crystal. The variation of the Bragg's angle due to the curvature allows to focus the beam in a region smaller than the size of the tile. <i>Right:</i> Representation of the maximum and minimum Bragg angle for a curved crystal. Blue arrows are the incoming radiation, while the red arrows give the direction of the local average diffracting plane.	24
2.7	Efficiency of a perfect curved crystal of Silicon as function of the curvature radius normalized to the critical radius, as valuated according to the Malgrage theory. The diffracting planes used are the (111) and the energy is fixed at 150 keV. The shape of the curve, however, does not depend on the energy.	26
2.8	Critical radius as function of the energy for Si(111) and Ge(111). We can clearly see that the critical radius increases as a power law with energy.	27
2.9	Optimal thickness vs Energy plot for a perfect bent crystal of Ge(111). The thickness is evaluated for different values of quasi-mosaicity. The optimal thickness increases as function of energy.	29
2.10	Representation of the branching of the incoming beam inside a crystal in the case in which the crystal is divided in four lamellae. The numbers represent the misalignment of every branch with respect to the previous is in fraction of δ_0 . The red branch in figure has a total misalignment of $-\delta_0$ with respect to the incoming beam. The physical angle of diffraction are the same for every branch, but they have been slightly changed in the drawing for clarity.	32

2.11	Extinction length in crystal of Silicon as function of energy for the families of diffracting planes (111), (333), (444) and (555).	35
2.12	Evaluated reflection efficiency as function of energy for a crystal of Germanium. The efficiency for the (111) planes is plotted from 140 keV to 610 keV, while the efficiency for the (333) planes is shown from 420 keV to 610 keV.	36
2.13	Reflection efficiency as a function of energy for a Silicon crystal. The efficiency for the (111) planes is plotted from 50 keV to 355 keV, while the efficiency for the (333) planes is shown from 150 keV to 355 keV.	36
3.1	Scheme of the libraries used in the LLL software, including relevant input and output parameters.	38
3.2	Section of the LLL GUI with an example of the type of <i>Tkinter</i> widgets used.	40
3.3	The new Graphical User Interface of the <i>Laue Lens Library</i> simulation software.	41
3.4	The "General Options" panel of the GUI.	42
3.5	The "Lens Configuration" panel of the GUI.	42
3.6	The "Crystals' Parameter" panel of the GUI.	43
3.7	The "Lens Parameters" panel of the GUI.	44
3.8	The "Source Parameters" panel of the GUI.	44
3.9	A 3D view of the designed NFT focal plane detector made with MEGAlib.	47
3.10	Experimentally measured energy resolution for a CZT based detector as function of energy. The red line is the linear best fit. The best fit parameters have been used in our software to take into account the energy resolution of a CZT based focal plane detector. Reprinted from Kuvvetli (2003).	48
3.11	Simulations of the redistribution profile for three monochromatic energies: 60 keV (purple curve), 300 keV (green curve), 600 keV (blue curve). The photopeaks corresponding to each respective energy are evident and dominate the spectrum. Nevertheless Compton events and photons escaped from the detector are present and contribute to off diagonal shape of the redistribution matrix.	50

3.12	The RMF fits file structure containing the information of the redistribution matrix. <i>Top</i> : the first extension where the redistribution matrix is stored (matrix column in which only the first element for each row is visible). Only 10 rows out of 550 are shown. <i>Bottom</i> : the second extension stores the <i>Ebound</i> (energy bounds) information describing the relation between channels and lower and upper energy threshold for each channel. Only 10 rows out of 512 are shown.	51
3.13	The effective area binned at 1 keV for the NFT. The jump in the effective area at 150 keV comes from the contribution of the Si(333) planes, while the jump at 510 keV comes from the effect of the Ge(333) planes.	52
3.14	The background level for ASTENA. This was extrapolated to Low Earth Orbit (LEO), foreseen for ASTENA, from the measurements of INTEGRAL/SPI operating in a high Earth orbit.	52
3.15	Spectrum of the Crab as it would be observed in the energy range 50-600 keV with ASTENA/NFT, with 3000 s integration time. The model is a photoelectrically absorbed power law. The lower panel shows the residuals between data and model in units of sigma.	53
4.1	Example of a parabolic X-ray mirror based on the grazing incidence technique.	56
4.2	Representation of Kirkpatrick-Baez mirrors. The first mirror focuses the radiation in the vertical direction, while the second focuses the radiation in the horizontal direction. The result is that the radiation is focused on a point.	57
4.3	Simulation of the PSF of a single diffraction Laue lens made by 10 rings of perfect, bent crystals for various off-axis sources. The energy band of the lens is 200 - 400 keV. The effect of the comatic aberration is evident even for small off-axis angles. The white circle represent the PSF area, centered on the centroid of the distribution, in which 50% of the photons are found. The dashed circle is the optimized circle in which 50% of the photons are found, without the constraint that the circle must be centered on the peak of PSF.	58
4.4	3D representation of a system of two curved crystals coupled. The beam impinging on the whole crystal is first focused by the upper crystal, then the lower crystal further diffracts the beam. At the end, the beam is focused on both directions.	59

4.5	The effect of two diffractions on the direction of the beam. The first diffraction rotates the beam on the z-y plane by an angle of two times the Bragg's angle. The second diffraction rotates the beam on the z-x plane.	60
4.6	Comparison of the Point Spread Function of a ring of single crystals (left) vs a ring of coupled crystals (right). The simulated crystals are bent mosaic crystals with a mosaicity of 15 arcsec and the focal length is 15 m. The improvement in image quality in the case of coupled crystals is evident. . . .	61
4.7	Simulations of the behaviour of a double diffraction Laue lens in the case of an on-axis source and two different off-axis sources. The simulated on-axis energy band is 200 – 600 keV. The left plots show the area of the lens which is active in the various cases, with the color encoding the photon energy from low (200 keV, red) to high (600 keV, blue). The right plots are the corresponding Point Spread Functions, with the ray-tracing of photons of different energies (color). The focal length is 15 m. We can see that the active area decreases as the off-axis angle increases, while the PSF is not significantly changed. Note that the dark violet color in these cases indicates non-active areas of the lens.	62
4.8	Simulated values of the HPD of a double diffraction Laue lens for some values of the off-axis angles.	63
4.9	Visual representation of the effective area of two coupled crystals. The total active area of the couple of crystals is given by the intersection of the active areas at a given energy on the two crystals. The total effective area is a thin, diagonal region.	64
4.10	Ray-tracing simulation of the active area for two coupled bent mosaic crystals. The photons are color-coded on the base of their energy, from lower (red, 158 keV) to higher energies (blue, 162 keV). The two crystals have a cross-section of $10 \times 10 \text{ mm}^2$ and a mosaicity of 15 arcsec.	65
4.11	Experimental configuration of the two coupled crystals. <i>Left photo</i> : side view of the crystals. The quartz frame on which one of the two crystals is glued is the sheet on the left side, while on the right side one can see the rotatable sample holder with the adjustable crystal. <i>Center photo</i> : front view of the coupled crystals. <i>Right photo</i> : the imager detector and the spectrometer used in our experiment.	66

- 4.12 *Top*: Diffracted images produced by the two crystals separately. The fixed crystal is oriented to an angle of $+45^\circ$, while the other is oriented to an angle of -45° . The observation time is 300 sec for both images. *Bottom*: Measured spectra of the beams diffracted by the two crystals separately. The signal by the fixed crystal is centered around 163.6 keV, with FWHM of 7.0 keV. The signal of the adjustable crystal is centered around 163.3 keV and its FWHM is about 5.8 keV. . . . 67
- 4.13 *Top*: Diffracted image produced by the two overlapping crystals. The integration time is 3000 sec. *Bottom*: the diffracted beam detected by the HPGe spectrometer. The signal is centered around 163.5 keV with a FWHM ≈ 3 keV. 68
- 4.14 Plot of the count rate of the double diffracted beam for various off-axis angle of the source. 69

List of Tables

2.1	Chosen value of quasi-mosaicity and thickness at various energy intervals for Germanium crystals.	28
2.2	Chosen value of quasi-mosaicity and thickness at various energy intervals for Silicon crystals.	29
4.1	Results of the off-axis performances test for two coupled crystals. The "Energy" column show the spectrum's centroid of the diffracted beam.	69

Introduction

The need for new instruments for High Energy Astrophysics

The field of High Energy Astrophysics is fundamental to understand phenomena on both stellar and cosmological scales. In the last sixty years of existence of HE Astrophysics, vast improvements in the sensitivity of the instrumentation have been made, thus allowing the study of the physics of many X-/Gamma-Ray sources with increasing details. However, there are still many open cases whose solution requires an increase in the sensitivity of the instrumentation. Just to cite some relevant examples, the nature of the 511 keV e^+/e^- emission at the galactic centre is still a mystery (Weidenspointner et al. 2008). We lack high-energy instruments with enough spatial resolution to understand whether the emission is diffuse or the result of the emissions of many unresolved point-like sources. Another interesting case is the robust modelization of Type-Ia and core-collapse supernova explosions, which require more precise data to distinguish among the various proposed models. Lastly, we cite the case of Gamma Ray Bursts (GRBs), among the most energetic phenomena in the Universe, whose mechanisms behind the generation of the prompt emission and afterglow are not totally understood. Their large luminosities make them excellent probes of the Universe in the era when the first stars formed, a few hundred million years after the Big Bang. To date, we have not being able to study the bulk of the low-luminosity population of GRBs, very few GRBs have been discovered in the first billion years of cosmic history, and polarization measurements have been rare and difficult. To advance studies in this field, new instrumentation is required, specifically the ability to focus hard X-rays (> 100 keV) using different techniques with respect to the grazing incidence mirrors utilised for low energy X-rays (< 80 keV, with significant sensitivity below 10 keV).

The ASTENA (Advanced Surveyor for Transient Events and Nuclear Astrophysics) concept mission, proposed to ESA for the "Voyage 2050" call (Frontera et al. 2019, Guidorzi et al. 2019) can be the answer to our needs. This mission will include two instruments: the Wide Field Monitor-

Imaging Spectrometer (WFM-IS), which will be a wide field instrument with both imaging and spectrometric capabilities, and the Narrow Field Telescope (NFT), which will be a narrow field instrument based on the concept of Laue lens (Frontera and Ballmoos 2011). The NFT is essentially a focusing lens based on Bragg's diffraction, built by combining dozens of perfect, bent crystals of Silicon and Germanium. Thanks to this instrument, we expect to reach unprecedented sensitivities both for continuum and line emission and to enable sensitive polarization measurements of celestial hard X-ray sources.

When focusing X-ray telescopes with grazing incident mirrors were introduced in the sixties (Giacconi 2010), at energies below 10 keV, X-ray astronomy blossomed. With a three orders of magnitude increase in the sensitivity of observations, X-ray missions such as *Einstein*, *ROSAT*, *Chandra*, *XMM-Newton*) to mention just a few, brought a revolution in our understanding of the Cosmos, revealing the crucial roles of stellar to supermassive black holes in the formation and evolution of the Universe, providing new ways to map the large scale structure, and ultimately opening the field of relativistic astrophysics. Similarly, the successive development of focusing techniques at energies above 100 keV, would bring a factor ~ 1000 jump in sensitivity, thus opening a new territory for astrophysics in the hard X-ray/soft γ -ray regime.

My work in this thesis is focused on the conceptual development of AS-TENA/NFT system. In particular, I will use simulations and experimental activity at the LARIX laboratory ([LARIX website](#)) to support the development of both the experimental techniques and the physical processes behind the Laue lens technology.

Thesis Organization

In the first Chapter, the state of art of the observations behind today's hottest topics in HE Astrophysics will be thoroughly discussed. First, the 511 keV diffuse emission from the Galactic center will be discussed, from its first detection in the '70s, to the most recent measurements by INTEGRAL/SPI, and the different interpretation proposed for the observations will be described. Then nuclear lines emission from supernovae will be described and we will see how the study of those lines can give an insight on the explosion physics. We will then turn into the case of fast transients such as GRBs. We will see how new and more precise polarization measurements can shed light on the physics of the prompt Gamma emission from GRBs and how new hard X-/soft γ -rays instruments can help us to study their afterglow in unexplored energy bands. Understanding the nature of the progenitors of GRBs is very active line of research. The recent discovery that some type of GRBs are the electromagnetic counterparts of gravitational wave events has opened the era of multi-messenger

astrophysics. Finally, the scientific cases of other new and still mysterious classes of transients, such as Low Luminosity GRBs, Fast Blue Optical Transients, Fast Radio Bursts and more, will be described and we will see how new instrumentation will be critical to improve our understanding of those phenomena by identifying potential high energy counterparts.

In the same Chapter the ASTENA mission will then be described. We will illustrate the characteristics of the two main instruments aboard the mission, WFM-IS and NFT, focusing on the expected performances of the mission.

In the second Chapter, I will describe how we evaluated the reflection efficiency of the crystals composing ASTENA/NFT, which is a fundamental parameter for estimating the sensitivity and the effective area of the instrument. In this Chapter the basics of the physics of a Laue lens and of the type of crystals which we plan to use for NFT will be revised, then I will describe how we combined Malgrange's formula for strongly bent crystals and a computational algorithm developed by Bellucci et al. (2011) to create a Python code able to evaluate the reflection efficiency as function of the energy for perfect, bent crystals of Silicon and Germanium. I will also describe how we extended the same code to evaluate the contribution of higher order of diffraction by the same crystals. Those results have been used to optimize the distribution of the Silicon and Germanium tiles on the lens and to compute the sensitivity and the effective area of the NFT.

The third Chapter will be devoted to the simulations of the focal plane of the NFT and to the activities aimed at upgrading the Laue lens simulator tool developed at the University of Ferrara. The software upgrades of the Laue Lens Library consisted in the construction of a Graphical User Interface, which improves the ease of use and user-friendliness of the software. The main concepts behind GUI programming will be briefly illustrated and the new interface and its functionalities will be described. The simulation of the focal plane detector instead has been performed using the MEGAlib software. In this Chapter, I will also describe how we obtained the first simulation of the response matrix of the NFT detector, which is also the first attempt to construct a response matrix for a Laue lens based instrument. This is a new tool which opens the possibility to simulate observations with ASTENA/NFT, thus allowing the spectral analysis of the specific sources and phenomena, a crucial step to assess the feasibility of a number of science cases described in the first Chapter.

Finally, in the fourth and last Chapter, we will describe and discuss a new, innovative concept for a Laue lens: a double Laue diffraction scheme. This new configuration shows some very interesting properties, which can open new opportunities for X-ray and γ -ray imaging and expand the concept and potential applications of Laue lenses. In this Chapter, I will describe how two bent crystals can be coupled to obtain a double diffraction. Using ray tracing simulations, I will specifically show how this coupled

crystal configuration offers improvements in the Point Spread Function and off-axis performances over the single crystal lens. In this Chapter, I will also present the first images obtained by two coupled crystals, produced at the LARIX facility of Ferrara, which indicates that the coupling is feasible and that the study of this configuration can lead to new instrumental capabilities in the future.

Chapter 1

ASTENA: A new instrument for X-Ray astrophysics

High Energy Astronomy is a key field for understanding the physics underlying astrophysical phenomena on stellar and cosmological scales. HE observations are crucial both for the study of transient sources, both for nuclear astrophysics. There are some relevant open cases in HE astrophysics, which would benefit from an improvement in the sensitivity of our instrumentation. The ASTENA concept mission proposed to ESA can be the answer to this necessity. In this Chapter we will describe what are those important open issues, then we will describe the ASTENA mission and how the technological improvement brought by ASTENA can help us to solve those cases.

1.1 Open cases in high energy astrophysics

From the birth of High Energy observations, dated 1962 (Giacconi et al. 1962) to the present days, the field of X and Gamma ray observations has come very far from its beginning, yet there are still some scientific cases which would greatly benefit from a further advancement of the instrumentation. In this section we will illustrate some of the main open issues and why we need new technologies to solve them.

1.1.1 The positron line puzzle: 511 keV annihilation emission from the Galactic Centre

The diffused 511 keV e^+/e^- annihilation line emission in the Galactic Centre (GC) was first detected in the '70s (Johnson et al. 1972, Leventhal et al. 1978) through balloon flights. In the following years, the emission has been widely observed by various instruments and satellites, including CGRO, WIND and INTEGRAL (Purcell et al. 1993, Teegarden et al. 1996, Weidenpointner et al. 2008). As seen in Fig. 1.1, recent data tell us that the emis-

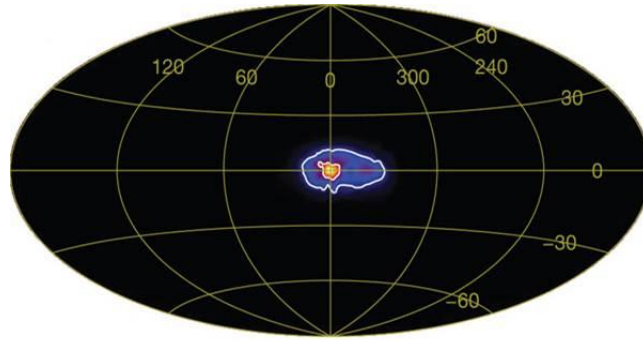


Figure 1.1: Map of the 511 keV emission line measured by INTEGRAL/SPI (Weidenspointner et al. 2008). The emission shows a symmetric central bulge and a clearly asymmetric diffuse disk.

sion shows a central, highly symmetric bulge and strongly asymmetric disk emission with an enhancement at positive latitudes (Weidenspointner et al. 2008, Skinner et al. 2015). At the moment, the asymmetry is still not confirmed, since this finding is in contrast with other results which found the emission to be symmetrical (Bouchet et al. 2009). The total estimated flux for the whole Milky Way is $(2.7 \pm 0.3) \times 10^{-3}$ photons $\text{cm}^{-2} \text{s}^{-1}$, which translates in an annihilation rate of 5×10^{43} $e^+ e^- \text{s}^{-1}$ (Siegert et al. 2016).

The debate on what can be the source of this emission is still open and active. At the moment, the sensitivity of our instruments does not allow us to understand if the emission is a diffuse emission or the unresolved emission of many point-like sources. The most promising candidate discrete sources are Low Mass X-Ray Binaries populating the regions around the Galactic Centre. The emission would be generated by pair annihilation happening in jets and by photon-photon interaction in the accretion disks of the binaries. Other possible discrete sources for the emission are dense clusters of stars, such as clusters of flaring M- to G- type stars or globular clusters, which can account for the 511 keV emission, or the decay from radioactive ejecta in Core Collapse Supernovae. On the other hand, it has also been advanced the hypothesis that the emission is truly diffuse and some studies have tried to suggest that it could be the product of the decay of Dark Matter particles in Standard Model Particles (Bøhm 2009). The current instrumentation lacks for the necessary sensitivity to be able to resolve the region of the GC and distinguish eventual point-like sources: with INTEGRAL/SPI we reach an angular resolution of $\sim 2.7^\circ$ (Vedrenne et al. 2003), which is not enough for further studies of the 511 keV emission.

The ASTENA mission however could be the answer to our problem: with its unprecedented expected sensitivity of $\sim 7 \times 10^{-6}$ in 1 Ms, it will be able to distinguish between the diffuse vs discrete origin of the emission and to accurately map its spatial distribution, giving us a new understand-

ing of the nature of the 511 keV emission.

1.1.2 Physics of Type-Ia and core-collapse supernovae

Measurement of the continuum and line emission in the spectra of both Type-Ia and core-collapse SNe is fundamental to describe the mechanism underlying those phenomena and discriminate between the various models of explosion. The origin of those two types of SNe is different, so we discuss them separately.

Type-Ia SNe are generated by the thermonuclear explosion of white dwarfs in binary systems accreting mass from a main sequence companion star or by merging of white dwarfs. Type-Ia SNe have an important role in cosmology since they are one of the most important distance indicators thanks to the Phillips empirical relation, which relates the peak intensity of the SN emission to its total duration. The explosion mechanism is still not totally understood and various models have been suggested (Fig. 1.2), while we know with a significative certainty that the main source of energy which powers the lightcurve of Ia SNe is the decay chain $^{56}\text{Ni} \rightarrow ^{56}\text{Co} \rightarrow ^{56}\text{Fe}$ in which the first decay has an half-life of 6.1 days and the second of 77.7 days (Churazov et al. 2014, Diehl 2015).

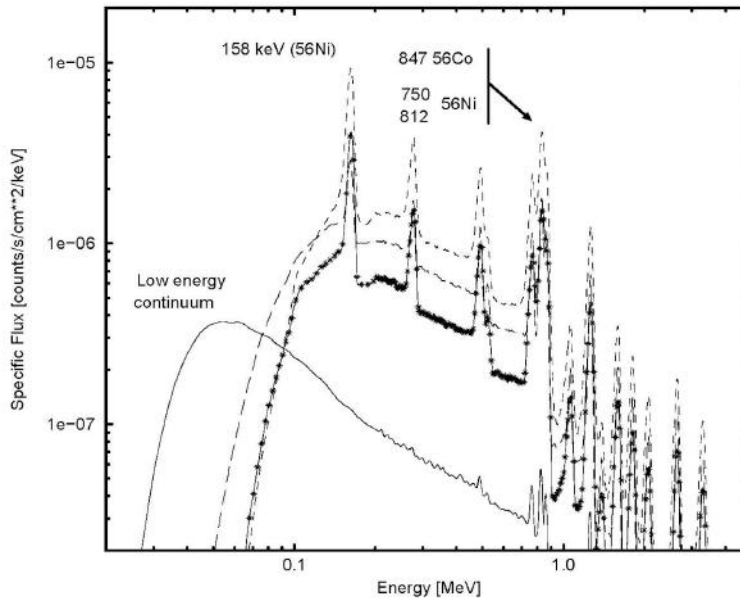


Figure 1.2: The expected gamma ray spectrum for a Ia SN at 20 days of the explosion, according to different models for the explosion mechanism. Reprinted from Gómez-Gomar et al. (1998)

The strongest lines above the continuum spectrum are the 158 keV and 812 keV ^{56}Ni lines and the 847 keV and 1238 keV lines from ^{56}Co . Studying both the continuum and the lines can give us a significant insight on what happens during a SN. The best approach is to study the 158 keV, since the resolution at very high energies is lower and it can be hard to distinguish between the 812 keV and the 847 keV lines. At the moment, the estimated line sensitivity of INTEGRAL at 150 keV is of $(1.1 \pm 0.4) \times 10^{-4}$ photons $\text{cm}^{-2} \text{s}^{-1}$ (Diehl et al. 2014) in 150 ksec; with ASTENA, we will be able to reach a sensitivity of approximately 10^{-6} photons $\text{cm}^{-2} \text{s}^{-1}$ in 1 ksec of observations. This means that with ASTENA we will be able to detect lines from fainter SNe and will be able to study a greater number of SNe per year up to a distance of 120 Mpc. This huge amount of data will improve our understanding and modelization of Ia SNe, but not only: ASTENA will also allow us to increase our knowledge of core-collapse SNe.

A core-collapse SNe represents the final stage of the life-cycle of massive stars. During those events, the extreme temperatures and pressures allow for the synthesis of many heavy elements. The mass quantity and spatial distribution of elements which are formed in the SN is directly related the explosion's mechanisms and structure, so the study of the products can probe the physics of the SN itself. One of the most observed element is the ^{44}Ti , whose decay chain is $^{44}\text{Ti} \rightarrow ^{44}\text{Sc} \rightarrow ^{44}\text{Ca}$, with half-life of 58.9 ± 0.3 yrs (Ahmad et al. 2006). ^{44}Ti emits lines at 4.1, 67.9, 78.4, 511 and 1,157 keV, which become visible once the ejecta is optically thin, and is produced in the innermost regions of the SN, thus it is one of the best probes of the explosion mechanisms. With the NuSTAR satellite we were able to study the spatial distribution of the lines, and the corresponding mass distribution, of the produced ^{44}Ti across the remnant of Cassiopeia A (Grefenstette et al. 2014, 2017), obtaining results that suggest the existence of intrinsic asymmetries and clumpiness inside the explosion.

Increasing the instrumentation capabilities above the limit set by NuSTAR would allow new and deeper studies of the interiors of Supernovae explosions. With ASTENA NFT we expect to achieve an angular resolution similar to NuSTAR (which has a resolution of 58 arcsec, Harrison et al. 2013) and a greater sensitivity. This will allow us to perform accurate studies of the distribution of lines in remnants and detect a lot of newly created elements in the event of a close neutron star merger or a Galactic SN, thus improving our knowledge of the burning mechanisms of SNe.

1.1.3 Prompt emission and afterglows of GRBs

Besides Supernovae, there are other important classes of transient phenomena whose study would benefit from a technological upgrade. One of the most studied and known are the Gamma Ray Bursts (GRBs). GRBs are characterized by a short lived gamma-ray prompt emission and by a long

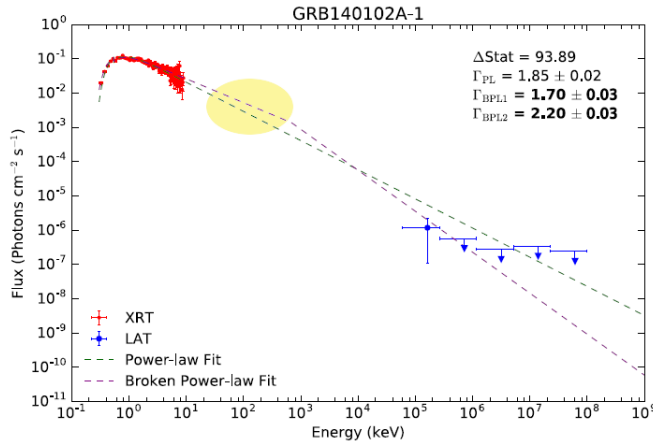


Figure 1.3: Afterglow data measured by Swift/XRT and Fermi/LAT. AS-TENA will cover the region highlighted in yellow. (Reprinted from Guidorzi et al. (2019), adapted from Ajello et al. (2018))

lived, broadband afterglow emissions. We distinguish two classes of GRBs based on the duration of the prompt emission: short GRBs last from tens of milliseconds to seconds, while long GRBs last from seconds to thousands of seconds. The light curves of both type are extremely variable and strongly non thermal, while the radiation is not emitted in a isotropic way, but in two collimated jets. The afterglow emission instead is in most part a synchrotron emission generated by the surrounding interstellar medium shocked by the GRB's blast wave and spans several decades of energies, from X-ray to radio (Kumar and Zhang 2015).

During the last fifty years, GRBs have been widely observed and studied, which allowed us to understand their key role as products of stellar evolution and binary mergers and possible synthesizer of heavy elements. Due to their high luminosity, they are also visible at higher redshifts than supernovae, allowing us to explore deeper regions in the sky. However, there are still important open questions on the nature of those phenomena. First of all, the mechanism which generate the prompt emission, how this propagates in the ejecta and the role of the magnetic fields are still not understood. A way to comprehend what lies behind a GRB is by studying the polarization of the prompt hard X and Gamma rays radiation, which is sensitive both to the type of emission mechanism and to the structure of the magnetic fields. At the moment, the study of GRBs polarization is still at an early phase: from the collective catalogue of various missions, including CGRO, INTEGRAL, Astrosat, (McConnell 2017) and from the recent data of the POLAR instrument (Zhang et al. 2019), we can see that the polarization has been measured for about a ten of GRBs, however the data are still at low significance and don't allow to discriminate between the vari-

ous proposed model for the prompt emission. The knowledge of the GRBs afterglow can also be improved by new data: at the moment, hard X-ray afterglow have been measured up to 60 keV using BeppoSAX/PDS, NuSTAR and INTEGRAL and in the range 100 MeV - 100 GeV by Fermi/LAT, however we lack for data between those two energy bands due to the low sensitivity of our instruments (Fig. 1.3). Last, another important open issue is the determination of the progenitors of those phenomena. The recent observation of the gravitational wave event GW170817 by the LIGO-VIRGO Collaboration and the identification of its electromagnetic counterparts in the short burst GRB170817A established that neutron star mergers are a family of progenitors for short bursts (Abbott et al. 2017). The possibility to study those mergers both with GW data and with the electromagnetic GRB counterpart open a whole new possibility in the study of both high energy transient physics, gravitational waves, fundamental physics and cosmology. In the future, by studying GW-EM pairs, it will be possible to have a precise localization of the host galaxy of the GW, allowing for precise redshift estimations, to obtain a new, independent way to estimate the Hubble constant (Guidorzi et al. 2017) and to probe fundamental physics laws and postulates such as the Lorentz invariance (Amelino-Camelia et al. 1998).

In the next decade we expect that a new generation of gravitational waves detector (Einstein Telescope, Cosmic Explorer, Laser Interferometer Space Antenna) will enter in function, so increasing the sensitivity of the our high energy instrumentation will increase the synergy between GW and EM observations. The ASTENA mission, with its Wide Field Monitoring Spectrometer (WFM-IS) and with its Narrow Field Telescope, can give us a new insight on all the above scientific cases. The WFM-IS polarimeter, thanks to its estimate Minimum Detectable Polarization (MPD) lower than 10% for energies < 300 keV and lower than 30% for energies < 600 keV, will allow us to measure the polarization level of a both the prompt emission and the afterglow of a vast number of GRBs and determine its temporal and energy dependence. This will give us a new insight on the physics underlying both type of emission and we will be able to discriminate between the various model proposed. In addition, the large field of view of WFM-IS (above 2 sr), its large effective area and its polarimetric capabilities will be crucial for a fast localization of EM counterparts of GW events, while the NFT will be able to follow up GRBs and their afterglow in an energy band which extends up to 600 keV. We expect that those data will be crucial in addressing the open issues described and that will increase our understanding of GRBs physics and of the fundamental physics involved.

1.1.4 Low Luminosity GRBs and other fast transients

New instruments can also help us to understand the nature of new, recently discovered, classes of transients. One category of long GRBs, in particular,

shows some interesting behaviours. Those are the low luminosity GRBs (ll-GRBs), which are characterized by a peak luminosity of $10^{47} - 10^{49}$ erg/s, in contrast with the luminosity of a typical GRB of $10^{50} - 10^{51}$ erg/s.

It has been observed that most of them are associated to Ic SNe, however for some of them we have not found an associated SNe (Fynbo et al. 2008). The study of those GRBs could help us in understanding the link between Gamma Ray bursts and regular Supernovae, investigating the possibility that also long GRBs could be the product of SNe or Ipernovae. At the moment, due to their low luminosity, all the observed llGRBs are at low redshifts, however studies infer that their volumetric rates can be larger than the one of regular long GRBs (Liang et al. 2007). An instrument capable of more sensitive wide fields studies, such as the WFM-IS, could help us in detecting more of those class of objects and allow for an extensive study of their properties.

Another interesting, recently discovered, class of astrophysical objects are the Fast Blue Optical Transients (FBOPT), whose spectra, as their name suggests, shows a prominent emission in the blue and their peak luminosity can be as high as Ibc SNe luminosity (i.e. greater than 10^{43} erg/s). Their light curves show a very fast evolution, which is not compatible with the ^{56}Ni decay which we believe powers regular SNe (Pursiainen et al. 2018). The progenitors of those transients and their emission at various energy bands are still vastly unknown and newer and more significative data in hard X and Gamma ray could be necessary to understand the nature of those phenomena and the possible correlation with other transients, such as GRBs.

Fast Radio Bursts (FRBs) are also another interesting, new class of transients. They are bursts of radio waves with a duration of the order of 1 msec and smaller, which show a random distribution in the sky. At the moment, we detected above 80 FRBs and the redshift was measured for three of them (Tendulkar et al. 2017, Ravi et al. 2019, Bannister et al. 2019), indicating that they are at cosmological distances. At the moment, no solid evidence of X-ray and Gamma rays counterparts of those burst has been found, even though some models include the possibility of an associated high energy emission. Investigating this issue with more precise instruments can be very helpful in confirming or excluding those models.

Last, there is a number of unknown high energy transients, with a broad range of diverse physical properties, which have been discovered in the last years and whose nature is still not know. At the moment, they don't show common properties: their luminosities vary in the range $10^{40} - 10^{46}$ erg/s, while they durations vary from some seconds to hours. A new broadband, wide field survey can help us to localize more of them and understand their physical origin and properties.

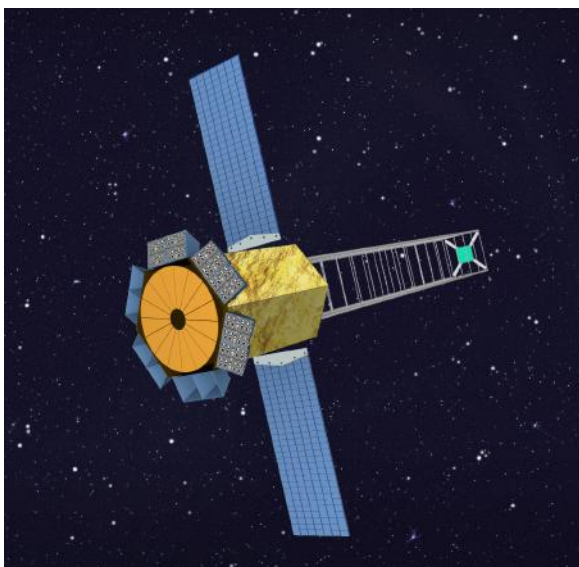


Figure 1.4: Artistic view of the ASTENA Spacecraft. Reprinted from Frontera et al. 2019

1.2 The ASTENA payload

In the previous section we discussed some important and open astrophysical cases in HE Astrophysics and how the expected performances of ASTENA would come in play. Following the whitepapers by Frontera et al. (2019) and Guidorzi et al. (2019), in this section we will illustrate more in details the characteristics of the mission, whose configuration is shown in Fig. 1.4, and the two main instrumentation on board: the Wide Field Monitor-Imaging Spectrometer (WFM-IS) and the Narrow Field Telescope (NFT).

1.2.1 Wide Field Monitor-Imaging Spectrometer (WFM-IS)

The WFM-IS is made up by twelve detection units surrounding the hexagonal body of the spacecraft and each detection unit is made by a Position Sensitive Detector (PSD) topped by a coded mask (Fig. 1.5). The PSD is an array of 4×8 modules and each module consists in ten rows of hexagonal scintillator bars, for a total of 205 bars per module. In the current project, the bars will be made by CsI(Tl), will be measuring 4.5 mm between flats and the length will be optimized in order to exploit the Compton interactions in different bars to its full potential. Each bar will be topped by a linear multi-anode Silicon Drift Detectors (SDD) with a thickness of 0.4 mm, while on the bottom an hexagonal, 4.5 mm between flats, single-anode SDD will be placed (Fig. 1.5). The coded mask is double scaled: one mask will

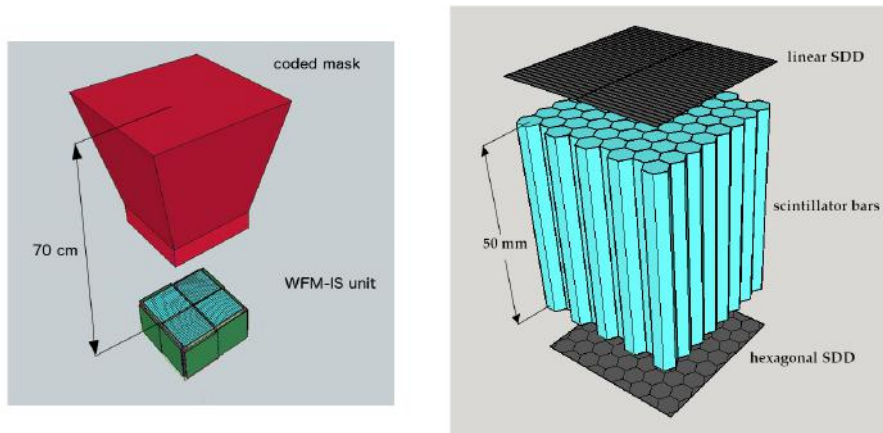


Figure 1.5: *Left*: Schematization of a single detection unit of the WFM-IS. The whole instrument is composed by 12 detection units.

Right: Schematization of one of the module composing the detection units of WFM-IS. Each unit is an array of 4 x 8 modules.

be made in Tungsten, 1 mm thick and will work in the energy range 30 - 150 keV. This mask will have a 2-D 43 x 41 elements basic pattern of 10 x 10.1 mm. The other mask will be dedicated to energies lower than 30 keV and will consist in a 0.5 mm thick, stainless steel, 1-D pattern mask. Thanks to this configuration, WFM-IS can work in an energy passband of 2 keV - 20 MeV and can achieve a field of view of 2 sr, with an angular resolution of 6 arcmin. The total effective area reached by the instrument is about 5800 cm² for energies smaller than 30 keV, about 6700 cm² in the energy range 30 - 150 keV and 13800 cm² above 200 keV. The minimum detectable polarization as function of the energy for WFM-IS is shown in Fig. 1.6. As we already described, those properties of the WFM-IS will allow for new wide field surveys and unprecedented studies on the polarization of HE radiation.

1.2.2 Narrow Field Telescope (NFT)

The NFT consist in a Laue lens telescope with a diameter of about 3 m and a focal length of 20 m. A Laue lens consists in a spherical lens made of hundreds of crystal tile which is able to focus high energy radiation exploiting the Bragg's diffraction in transition geometry (Frontera and Ballmoos 2011). The lens will be made by ~ 19500 perfect crystal tiles of Si(111) and Ge(111), bent to a curvature radius of 40 m (5% tolerance), allowing for a total passband of 50 - 600 keV. The tiles' dimensions are 30 x 10 x 2 mm and their misalignment with respect to the diffraction position must be smaller than 10 arcsec. The physical principle of a Laue lens are described more in detail in the second Chapter. The technology to bend the crystals and

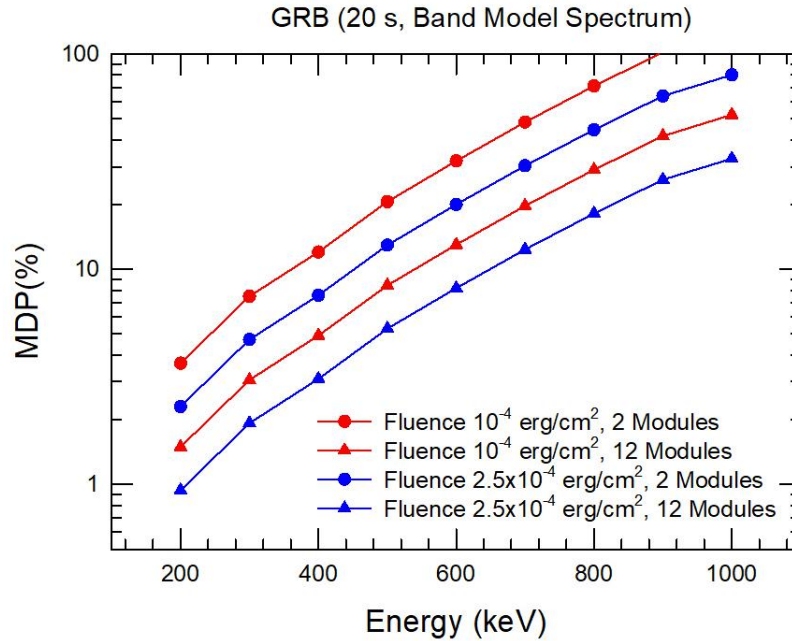


Figure 1.6: Minimum detectable polarization at 3σ for the WFM-IS. The MDP is evaluated for a GRB with a duration of 20 s and two different value of fluence. The assumed spectrum of the GRB is a Band law with typical values $\alpha = 1.0$, $\beta = 2.3$ and peak energy of 300 keV.

to assemble the lens was developed in the contest of the LAUE project; the expected performance of the lens has already been simulated (Virgili et al. 2015, 2017) and the increase of the technological readiness, with the development of a first lens prototype, is the goal of the Technological Readiness level Increase for Laue Lenses (TRILL) project.

The focal plane detector instead is a solid state PSD made up by 4 layer consisting in 4×16 , 2 mm thick, CdZnTe (CZT) elements, with a cross section of 0.2×2 cm 2 . The total cross section is of 8×8 cm 2 and the total thickness is 8 cm, allowing for an efficiency higher than 80% (Kuvvetli et al. 2014, Auricchio et al. 2012). In this configuration, NFT will reach a projected geometrical area of 7 m 2 and we expect to reach an extraordinary continuum and line sensitivity (Fig. 1.7 and 1.8, estimated for an observation time of 10^5 sec), which will also allow the NFT to work as a polarimeter in the 100 - 600 keV range, exploring the almost unknown regions of hard X and Gamma rays polarimetry. This new focusing instrument based on diffraction techniques will bring an increase in the sensitivity for hard X-rays (>100 keV) of a factor ~ 1000 , which is comparable with the increase in sensitivity in the soft X-ray band (<10 keV) which was brought by the first grazing incidence focusing instruments, such as Einstein, ROSAT, Chandra

and XMM-Newton (Giacconi 2010). The use of grazing incidence technique revolutionized the field of HE astrophysics and provided a new and more sensitive way to study the X-ray sky. We expect that ASTENA will bring the same revolution in the hard X-ray band, opening a new field of possibilities for HE observations.

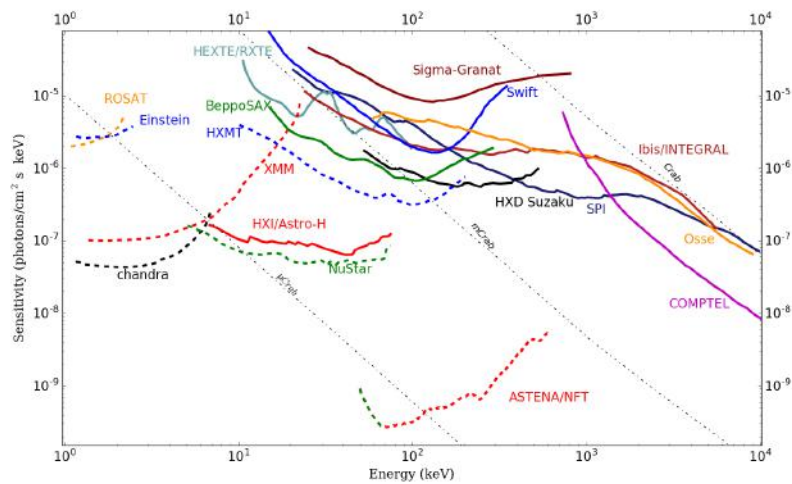


Figure 1.7: ASTENA/NFT continuum sensitivity compared to other past or current missions for an observation time of 10^5 s.

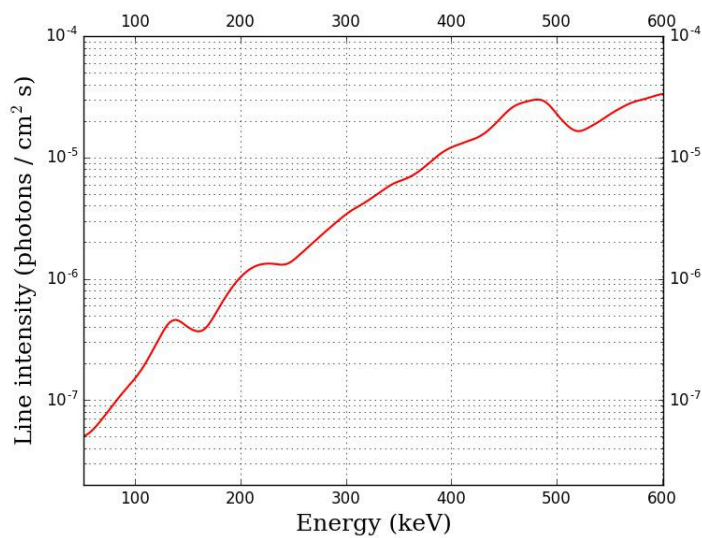


Figure 1.8: Estimated line sensitivity for ASTENA/NFT for an observation time of 10^5 s.

Chapter 2

Efficiency of Si and Ge crystals for the Laue lens of ASTENA/NFT

The Narrow Field Telescope that will be part of the ASTENA satellite is a Laue Lens, which is a lens able to deflect and focus high energy radiation using Bragg's law of diffraction. In this Chapter we will describe the main properties of a Laue Lens and of the crystals which can be used to build it. Next we will describe the method we used to evaluate the reflection efficiency of the crystals which we plan to use to build the ASTENA-NFT and, consequently. The evaluated reflection efficiency will allow us to estimate the sensitivity of the lens.

2.1 Bragg's Law of Diffraction and Laue Lenses

Laue lenses are based on the Bragg's law of X-ray diffraction in crystals. In a crystalline material with interplanar spacing d_{hkl} , the Bragg's law is:

$$2d_{hkl} \sin \theta_B = n \frac{hc}{E} \quad (2.1)$$

Where θ_B is the angle between the direction the lattice planes and the diffracted photon, E the energy of the photon, n the order of diffraction and $hc = 12.4 \text{ keV} \cdot \text{\AA}$ (Zachariasen 1945) (Fig. 2.1). Depending on how the lattice planes are oriented with respect to the surface of the crystal, we can define two possible geometries:

- **Bragg (or Reflection) Geometry:** in this configuration the lattice planes are parallel to the surface of the crystal. If we imagine that the crystal divides the space in two separate regions, in this configuration the diffracted beam can be found in the same region of the incident beam (Fig. 2.2, left).

- **Laue (or Transmission) Geometry:** in this configuration the lattice planes are orthogonal to the surface of the crystal. In this case the beam crosses the crystal and can be found in the region of space over the crystal (Fig. 2.2, right).

Using Bragg diffraction, we can then deviate the radiation that hits a crystal and redirect it to a point of our choice. This principle is what we use for the construction of Laue lenses, which are spherical lenses made of crystals in transmission configuration (Frontera and Ballmoos 2011). We can visualize a Laue lens as an "umbrella", i.e. a spherical cap, covered in crystal tiles whose diffracting planes are perpendicular to the surface of the sphere (Fig. 2.3). In this configuration, the focus of the lens is located on the symmetry axis of the lens, at a focal distance f equal to half the curvature radius R of the spherical cap. If we call r the distance from the axis of the lens at which a tile is located, we can see that the Bragg's angle between the radiation and the crystal can be written as:

$$\theta_B = \left[\frac{1}{2} \arctan \left(\frac{f}{r} \right) \right] \quad (2.2)$$

Using the Bragg's law, we can see that the energy diffracted by the tile and the position r are related by the relation:

$$E = \frac{hc}{2d_{hkl}} \sin \left[\frac{1}{2} \arctan \left(\frac{f}{r} \right) \right] \quad (2.3)$$

In the case of high energies, the Bragg's angle are very small, so we can safely approximate the above equation to:

$$E \approx \frac{hc}{d_{hkl}} \frac{f}{r} \quad (2.4)$$

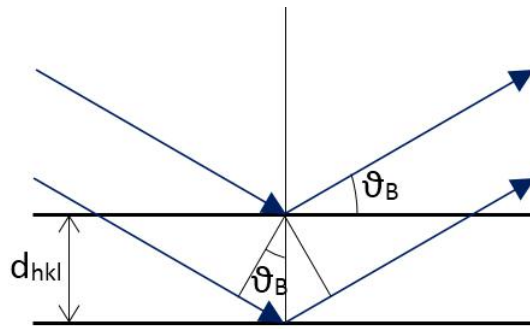


Figure 2.1: Schematic picture of X-ray diffraction in a crystal with interplanar spacing equal to d_{hkl} . Diffraction consist in an interaction between the photon and the periodic lattice structure of the crystal. The result of this interaction is that the incoming beam appears to have been deviated by the crystal to a new direction associated to the angle θ_B .

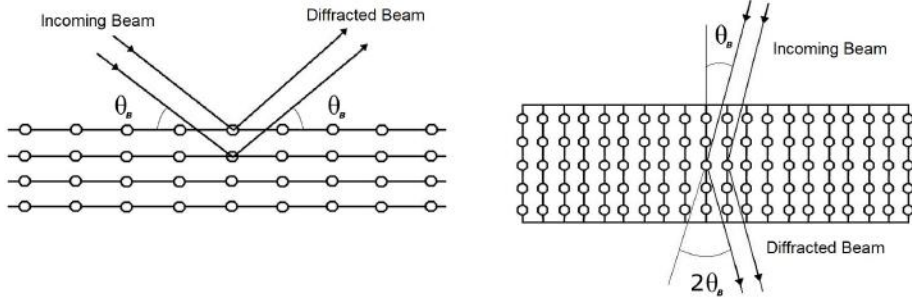


Figure 2.2: Schematic picture of a crystal in Bragg geometry (left) and Laue geometry (right).

The tiles can be disposed on the cup in rings or in a spiral; both configuration allows us to obtain a smooth variation of the effective area of the lens as function of the energy, so, for simplicity, in the following we will suppose that the crystals are disposed on concentric rings. In this configuration, all the crystals on a ring are oriented to be all corresponding to the same Bragg's angle. The energy passband $[E_{min}, E_{max}]$ of the lens can be evaluated from 2.4:

$$E_{min} \approx \frac{hc}{d_{hkl}} \frac{f}{r_{min}} \quad (2.5)$$

$$E_{max} \approx \frac{hc}{d_{hkl}} \frac{f}{r_{max}} \quad (2.6)$$

In which E_{min} and E_{max} are the minimum energy and the maximum energy diffracted by the lens, while r_{min} and r_{max} are the radius of the corresponding rings. It is clear that a Laue lens is effectively a focusing telescope, which means that the continuum sensitivity of a lens can be defined as:

$$I_{n_\sigma}^{min} = \frac{n_\sigma}{\eta(E)f(E)A_{eff}(E)} \sqrt{\frac{2B(E)A_f(E)}{T_{obs}\Delta E}} \quad (2.7)$$

Where we called:

- E the energy of the incoming radiation.
- n_σ the signal to noise ratio, which establish the confidence level of the measurement.
- $\eta(E)$ the detector efficiency as function of the energy.
- $f(E)$ the fraction of focused photons.
- $A_{eff}(E)$ the effective area of the instrument, which can be computed as the product between the geometrical area of the instrument and the reflection efficiency $\epsilon_R(E)$ of the lens.

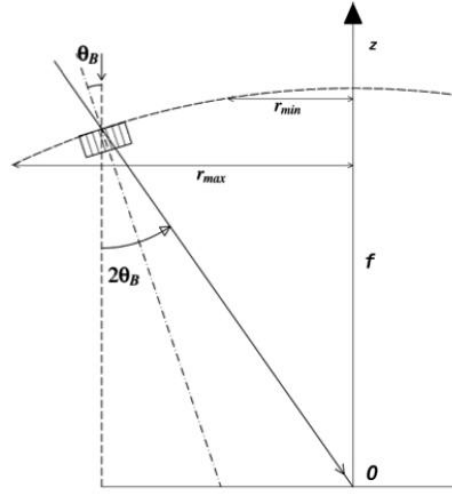


Figure 2.3: Schematic representation of a Laue lens. The Lens is a spherical cap with rings of crystals fixed above. All the crystals are oriented in such a way that the diffracted radiation is focused in the same point. The innermost ring with radius r_{min} diffracts higher energies, while the one with radius r_{max} reacts to the lower energies.

- $B(E)$ is the intensity of the background, measured in counts per unit area, time and energy.
- $A_{f(E)}$ is the detector area on which the fraction of the focused flux $f(E)$ falls.
- T_{obs} is the total observation time.
- ΔE is the energy band of the observation.

It is possible to separate the quantities which describe the geometry of the lens from the other quantities, independent from the telescope itself:

$$I_{n\sigma}^{min} = \frac{n_{\sigma}}{\eta(E)} \sqrt{\frac{2B(E)}{T_{obs}\Delta E} \frac{\sqrt{A_{f(E)}}}{f(E)A_{eff}}} = \frac{n_{\sigma}}{\eta(E)} \sqrt{\frac{2B(E)}{T_{obs}\Delta E} \frac{1}{\sqrt{S(E)}}} \quad (2.8)$$

Where we defined the equivalent surface $S(E) = (f(E)A_{eff})^2/A_{f(E)}$ that has the dimension of an area and depends on the energy. The equivalent surface will be also cited in the Chapter 3. Equally important is also the sensitivity to a narrow emission lines superimposed to the continuum which can be defined as:

$$I_L^{min} = 1.31n_{\sigma} \frac{\sqrt{[2B(E_L)A_{f(E)} + I_c(E_L)\eta(E_L)f(E_L)A_{eff}(E_L)]\Delta E}}{\eta(E_L)f(E_L)A_{eff}(E_L)\sqrt{T_{obs}}} \quad (2.9)$$

Where E_L is the centroid of the line intensity function, $I_c(E_L)$ is the source continuum intensity at the line centroid, ΔE is the full width at half maximum of the line profile and the other parameters are the same previously defined. To evaluate both continuum and line sensitivity, we need to compute the effective area of the lens, which require to know the total reflection efficiency $\epsilon_R(E)$ at a given energy. The efficiency depends on the type and the structure of the crystal which constitutes our lens, so, in order to evaluate the efficiency, we will study the diffraction in the type of crystals that we aim to use for the ASTENA-NFT, i.e. curved perfect crystals of Silicon and Germanium.

2.1.1 Diffraction in Perfect Crystals

A Flat Perfect Crystal (FPC) is a crystal whose lattice planes are all oriented in the same direction. Those crystals allows for Bragg's X-Ray diffraction, according to Eq. 2.1. In a FPC, the rocking curve is a narrow peak around the Bragg position. The Full Width at Half Maximum of this curve is called Darwin Width ($2\delta_W$ in symbols) and represents the broadening of the curve around the Bragg position. Following Authier (2003), the crystal thickness that leads to a complete suppression of the beam crossing the crystal (in Laue configuration) is called Extinction Length and is defined as:

$$\Lambda_0 = \frac{\pi V \cos \theta_B}{r_e \lambda C |F_h|} = \frac{\pi V \cos \theta_B}{r_e \lambda C |F_h|} \quad (2.10)$$

Where V is the volume of the unitary cell of the crystal, θ_B is the Bragg angle, r_e is the classic electron radius, λ is the wavelength of the diffracted radiation, C is the polarization of the radiation and $|F_h|$ is the so-called structure factor of the diffracting planes, which tells us how much the planes are effective in scattering the radiation. In Laue geometry, it is shown that the extinction length, the Darwin width and the interplanar spacing of the diffracting planes (d_{hkl}) are linked by the formula (Authier 2003):

$$\delta_W = \frac{d_{hkl}}{\Lambda_0} \quad (2.11)$$

The energy spectrum of the diffracted radiation will be constitute by a series of narrow peaks at the energies which satisfies the Bragg's law. Those type of crystals are very useful in the construction of instruments such as monochromators or single-line spectroscopy, but they are not the best choice for a focusing broad energy band instrument. The first reason is that flat crystal does not focus the radiation in the proper sense: the crystal is able to redirect the beam in a point of our choice, however the PSF produced by a flat crystal is at least of the same physical size of the crystal.

This comes from the fact that the Bragg's angle is the same in every point of the crystal, so the "shape" of the outgoing beam is conserved (Fig.

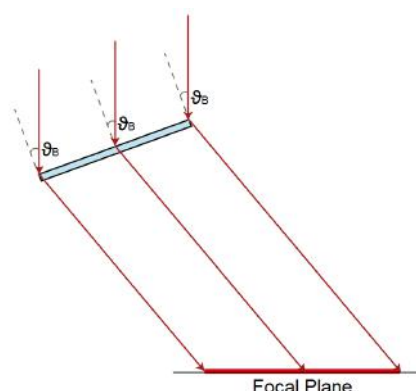


Figure 2.4: Image of a parallel beam generated by a flat crystal. The beam is redirected, but not focused. The resulting image has a size comparable with the size of the crystal tile.

2.4). This means that if we want to obtain a concentrated PSF, we would need to make very small crystals, which can be a hard task. The second problem arises from the fact that flat perfect crystals accept only a narrow band of energies: in an instrument such as a Laue lens, we want that the effective area is as high as possible and that the reflectivity of the lens varies in a smooth way with the energy, which means that the energy band of contiguous crystals have to overlap enough to guarantee what we need. However, the energy band accepted by flat perfect crystals is too narrow to allow enough overlap, so those crystals are not suitable for the construction of a broad band Laue lens. Last, the diffraction efficiency of flat crystals in Laue geometry can't be higher than 50% (Zachariassen 1945). This arises from the fact that in flat crystals, a photon has the same probability of undergoing an even or odd number of diffractions while traversing the crystal length, so at least half of the beam will be destroyed by the interference. A low efficiency can be a problem if we want to construct an instrument with a big effective area. A way to overcome those problems is to use Perfect Curved Crystals.

Perfect Curved Crystals

A Perfect Curved Crystal (PCC) is a crystal which has been dynamically or statically bent to a chosen curvature radius R_p , which is called external or primary curvature radius. This induces a secondary curvature of radius R_s on the internal diffraction planes of the crystal. This means that in PCC there is an angular spread of the planes, called quasi-mosaicity, so the Bragg's angle varies continuously while the radiation is crossing the crystal (Fig. 2.5). A crystal can be bent in various ways, but for our case we will consider statically bent crystal with a cylindrical curvature. We can see that

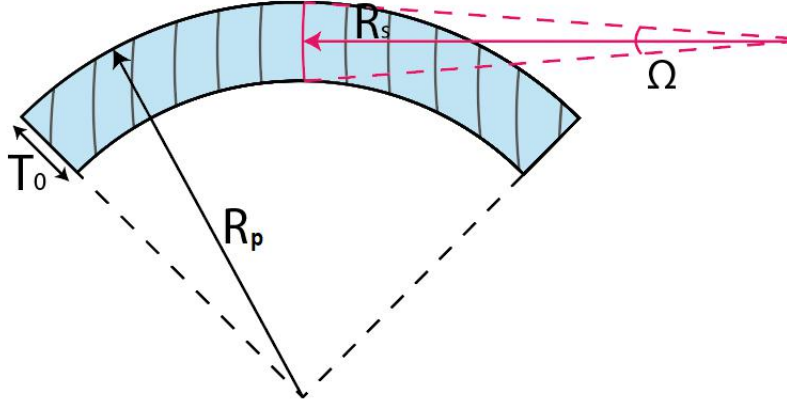


Figure 2.5: Representation of a perfect curved crystal. The crystal has a primary curvature radius R_p and the diffracting planes themselves show a secondary curvature radius R_s , which determines an angular spread of the planes Ω .

using those types of crystals allows us to overcome the issues we had with flat crystal.

First of all, the curvature allows us both to focus the radiation and to increase the energy band. To see this, for a moment we suppose to ignore the internal angular spread of the planes and we focus on the average direction of the diffracting planes in each point of the crystal. If the crystal is curved, the average direction of the planes changes in every point, which means that also the Bragg's angle for the radiation will be different in every point. The first evident effect of this variation is that the radiation beam is now squeezed in a region smaller than the size of the crystal, so the beam is effectively focused (Fig. 2.6, Left). Now we can have a look at how the curvature can increase the passband of a crystal. We call θ_M the average Bragg's angle of the crystal and $[\theta_M^{min}, \theta_M^{max}]$ the limits of the angular band of the crystal. If we call d the length of the crystal in the focused direction, we can see from geometric consideration that (Fig. 2.6, Right):

$$\theta_M^{min} = \theta_M - \alpha \quad (2.12)$$

$$\theta_M^{max} = \theta_M + \alpha \quad (2.13)$$

Where α is the angle subtended by half of the crystal. In the approximation in which the size d is way smaller that the curvature radius R_p of the crystal we can write:

$$\frac{d}{2R} = \sin \alpha \approx \alpha \quad (2.14)$$

This means that the angular spread of the Bragg's angle due to the primary

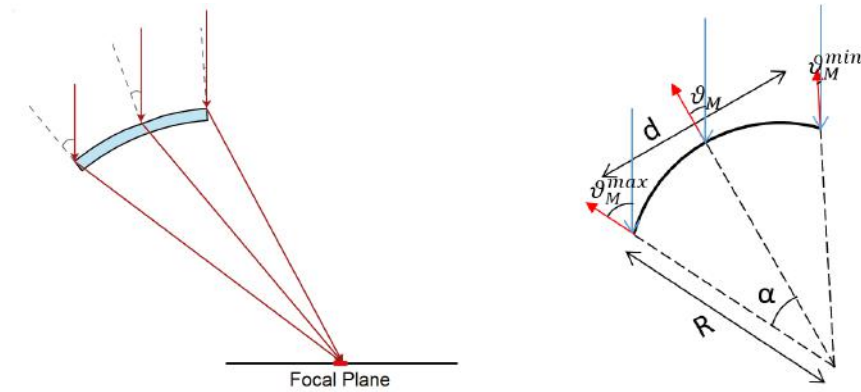


Figure 2.6: *Left*: Image of a parallel beam generated by a curved crystal. The variation of the Bragg's angle due to the curvature allows to focus the beam in a region smaller than the size of the tile. *Right*: Representation of the maximum and minimum Bragg angle for a curved crystal. Blue arrows are the incoming radiation, while the red arrows give the direction of the local average diffracting plane.

curvature can be written as:

$$\Delta\theta \approx \frac{d}{R} \quad (2.15)$$

Now, by deriving the Bragg's law in the small angle approximation, we can see that the following relation holds:

$$\frac{\Delta\theta}{\theta_M} = \frac{\Delta E}{E_M} \quad (2.16)$$

Where ΔE is the energy pass-band of a single crystal and E_M is the average energy diffracted. Inserting the Bragg's law and the expression for the angular spread that we obtained, we can rewrite the pass-band of a single crystal as:

$$\Delta E = \frac{2d_{hkl}}{hc} \frac{d}{R_p} E_M^2 \quad (2.17)$$

The energy pass-band for a curved crystal is then larger than the pass-band for a flat crystal, which was limited to a narrow region around the energy which satisfies the Bragg's law. From this, we see that the simple act of curving our crystals solved both the problem of the lack of true focusing and the problem of the narrow pass-band. It is worth noticing that the angular spread of the planes Ω is linked to the quality of the image produced by a crystal. To see this, we can consider a generic point on the surface of the crystal. If the planes of crystal were flat, in every point of the crystal there could be only one energy able to satisfy the Bragg's condition at first order. However the planes themselves are curved, which means that now

a single plane can be associated to more Bragg's angle, extending the local energy band in every point of the crystal. The consequence of this is that the size of the Point Spread Function of the crystal is enlarged and its new FWHM is equal to Ω .

At this point, we can also see that the curvature improve the reflectivity of the crystal, allowing us to overcome the 50% limit of perfect flat crystals. From an intuitive point of view, we can imagine that now that the planes are curved, the probability that the beam undergoes secondary interactions inside the crystal becomes lower, so the quantity of the beam which will be destroyed by interference will be lower. The mathematical formulation for the diffraction in strongly bent crystal is included in the Malgrange Theory.

2.1.2 Malgrange Theory for perfect curved crystals

The theory describing the diffraction inside perfect, homogeneously bent crystals in transmission configuration was developed by Malgrange (Authier 2003) from the dynamical theory of diffraction and is now well confirmed by experimental results (Keitel et al. 1999, Malgrange 2002). The parameters which describes the distortion of the diffracting planes is the so-called strain gradient β_S . In a crystal of thickness T_0 , with uniform curvature and angular dispersion of the planes equal to Ω , the strain gradient can be written as:

$$\beta_S = \frac{\Omega}{T_0(\delta_w/2)} \quad (2.18)$$

Where δ_w is the Darwin width of the crystal. At this point we define the critical strain $\beta_C = \pi/(2\Lambda_0)$ and a critical radius as:

$$R_c = \frac{2\Lambda_0}{\delta_w\pi} = \frac{2\Lambda_0^2}{d_{hkl}\pi} \quad (2.19)$$

Which was derived from the critical strain assuming that the curvature of the diffracting planes is given by $c_s = \Omega/T_0$. When the strain becomes larger than the critical strain, or analogously when the curvature radius of the crystal is smaller than the critical radius, the peak reflectivity of the crystal can be expressed as:

$$R^{peak} = \left(1 - e^{-\frac{\pi^2 d_{hkl}}{c_s \Lambda_0^2}}\right) e^{-\frac{\mu\Omega}{c_s \cos\theta_B}} \quad (2.20)$$

Where Λ_0^2 is the extinction length defined before and μ is the linear attenuation coefficient for the material of which the crystal is made. In the above formula, the second term represents the attenuation of the beam due to the self absorption of the material, while the first term represent the diffraction efficiency of the crystal, without the effect of the absorption. For small

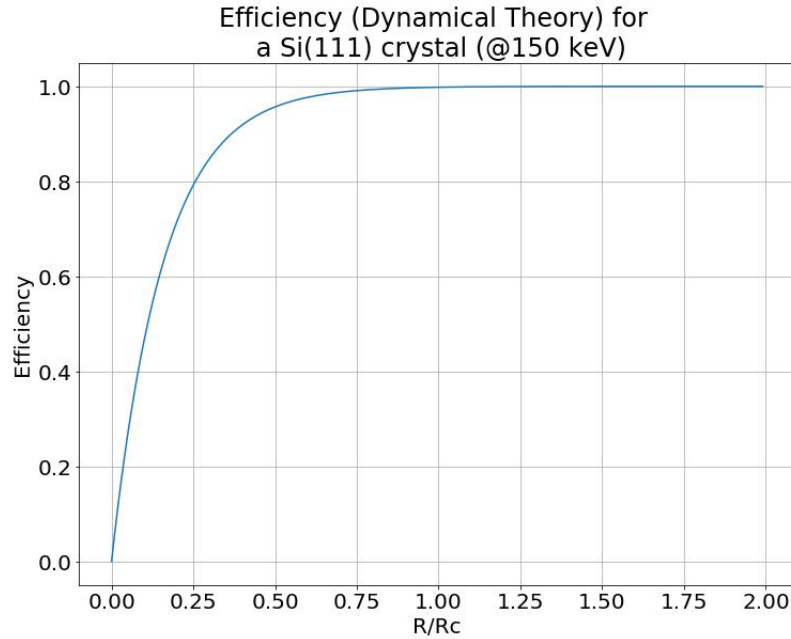


Figure 2.7: Efficiency of a perfect curved crystal of Silicon as function of the curvature radius normalized to the critical radius, as valuated according to the Malgrange theory. The diffracting planes used are the (111) and the energy is fixed at 150 keV. The shape of the curve, however, does not depend on the energy.

value of the quantity $1/c_s$, so for small curvature radius, the reflectivity can be approximated as:

$$R^{peak} \approx \frac{\pi^2 d_{hkl}}{c_s \Lambda_0^2} = \frac{\pi^2 d_{hkl}}{\Lambda_0^2} R_s \quad (2.21)$$

This means that when the crystal is strongly curved, the reflectivity depends linearly on the curvature radius. In the opposite limit, when the curvature radius increases and the crystal flattens, we would expect that the efficiency tends to 50%, while the efficiency given by the Malgrange theory tends to 1 (Fig. 2.7). This arise from the fact that when the curvature radius is close to the critical radius, the relation 2.21 cannot be used anymore and we will need to resort to alternative way to evaluate the reflectivity of a curved perfect crystal.

2.2 Modelling a crystal

To evaluate the performance of a Laue lens it is crucial to estimate the reflectivity of the single crystals of which it's composed. The aim of our cal-

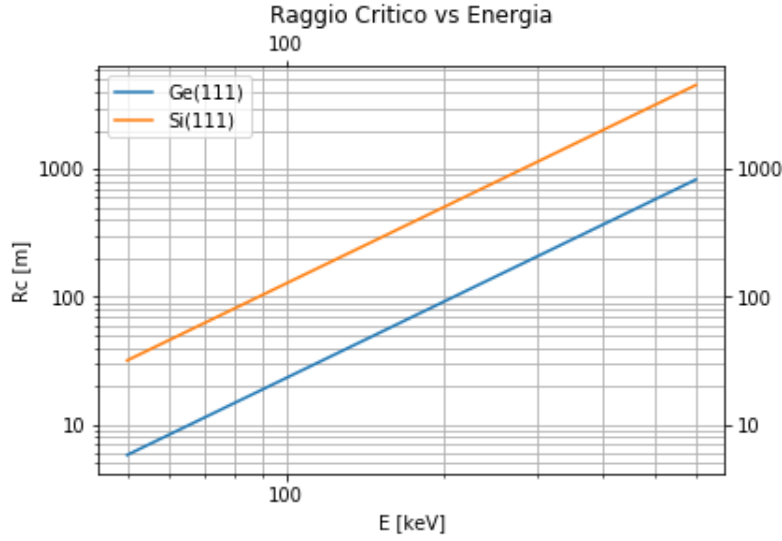


Figure 2.8: Critical radius as function of the energy for Si(111) and Ge(111). We can clearly see that the critical radius increases as a power law with energy.

culations is to estimate the efficiency of the crystals which will be made up of the ASTENA-NFT in the energy band [50 keV - 600 keV]. The materials chosen for the ASTENA-NFT are Silicon and Germanium and the chosen diffracting planes are the (111). Crystals are bent to a primary curvature radius R_p of 40 m. From previous results, it is known that the induced secondary curvature radius of the diffracting planes for the Germanium is equal to $R_s^{(Ge)} = 2.4 R_p = 96$ m, while it is $R_s^{(Si)} = 2.6 R_p = 104$ m.

We can evaluate the efficiency of the crystals using Malgrange's results as long as the curvature radius R_s is smaller than the critical radius. In the case of Germanium, the critical radius is greater than the curvature radius from about 200 keV and beyond, while for Silicon this happens at about 90 keV (Fig. 2.8). Below those two energy limits, we can't apply Malgrange's solution anymore and we must find an alternate way to evaluate the reflectivity of the crystal. The method that we will use to evaluate the reflectivity outside the strong curvature regime was developed by Bellucci et al. (2013) and it allows us to calculate the reflectivity for a crystal of arbitrary curvature radius. In both cases, we will work only with first order of diffraction for the Bragg's law, since the intensity of higher orders can be neglected.

When $R_s \ll R_c$, we can safely apply the Malgrange theory. From the results of Bellucci et al., we can see that the numerical calculation and the dynamical theory give the same result as long as $R_s \lesssim 0.4 R_c$. In order to be safe in applying the results of the dynamical theory, we decided to use the Malgrange formula only for $R_s < 0.3 R_c$. In this condition, the peak

reflectivity is simply given by Malgrange equation (Eq. 2.21). In order to increase the efficiency of the crystals, it can be worth the time to study which value of thickness gives us the greater peak reflectivity and take this in account while designing the lens. To do so, we recast the Malgrange reflectivity in the following way:

$$R^{peak} = \left(1 - e^{-\frac{\pi^2 d_{hkl} T_0}{\Lambda_0^2 \Omega}}\right) e^{-\frac{\mu T_0}{\cos \theta_B}} \quad (2.22)$$

We can show, through derivation, that the optimal thickness is given by:

$$T_0^{opt} = \frac{\ln(1 + \alpha/\beta)}{\alpha} \quad (2.23)$$

Where we defined:

$$\alpha = \frac{\pi^2 d_{hkl}}{\Lambda_0^2 \Omega} \quad (2.24)$$

$$\beta = \frac{\mu}{\cos \theta_B} \quad (2.25)$$

We can recast the optimal thickness to further evidence the dependence from the extinction length and the quasi-mosaicity of the crystals:

$$T_0^{opt} = \frac{\Lambda_0^2 \Omega}{\pi^2 d_{hkl}} \ln \left(1 + \frac{\pi^2 d_{hkl} \cos \theta_B}{\mu} \cdot \frac{1}{\Lambda_0^2 \Omega}\right) \quad (2.26)$$

Increasing the quantity $\Lambda_0^2 \Omega$, the optimal thickness becomes larger. The quasi-mosaicity is a constructive property of the crystal and does not depend on energy. The implicit dependence from energy arise from the contribution of the extinction length and the linear absorption coefficient. In our region of interest (from 50 keV to 600 keV), the linear absorption varies slowly both for Germanium and Silicon, without the presence of absorption edges, so the leading term in the optical thickness is the extinction length. For a fixed value of quasi-mosaicity, we can verify that the optimal thickness increases as the energy increases (Fig. 2.9). To choose the thickness of the crystals, we must also consider the followings:

Energy Range	Ω [arcsec]	T_0 [mm]
610 keV - 400 keV	10	5
400 keV - 350 keV	9	4
350 keV - 250 keV	7	3
Below 250 keV	4	2

Table 2.1: Chosen value of quasi-mosaicity and thickness at various energy intervals for Germanium crystals.

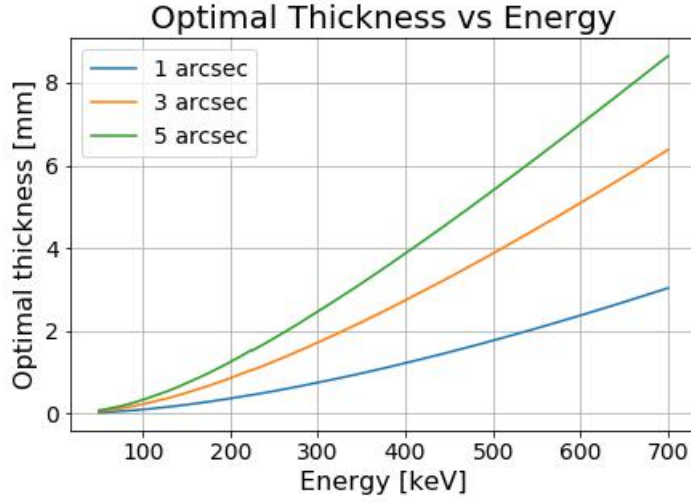


Figure 2.9: Optimal thickness vs Energy plot for a perfect bent crystal of Ge(111). The thickness is evaluated for different values of quasi-mosaicity. The optimal thickness increases as function of energy.

1. the curvature radius of the planes of the crystals is fixed by construction, so this gives us a constraint on the value of T_0/Ω , which must be equal to the chosen curvature radius.
2. At higher energies it can be useful to have larger values of Ω because this allows for a more stable effective area.
3. At the moment, there are some constructive limitations: we know that we can bend a crystal with sufficient precision up to thickness of 5 mm. This sets an upper limit on the thickness that we can choose. Very thin crystals can also be a problem due to excessive fragility. To avoid this, we choose the value of 2 mm as lower limit for the thickness.

To evaluate the optimal thickness, we choose a desired value for the quasi-mosaicity and then we applied Eq. 2.26. The chosen values of thickness

Energy Range	Ω [arcsec]	T_0 [mm]
350 keV - 200 keV	10	5
200 keV - 150 keV	8	4
150 keV - 130 keV	6	3
Below 130 keV	4	2

Table 2.2: Chosen value of quasi-mosaicity and thickness at various energy intervals for Silicon crystals.

T_0 , along with the quasi-mosaicity associate, are shown in Tab. 2.1 for Germanium and Tab. 2.2 for Silicon. When $R > 0.3 R_c$ we can't resort on the dynamical theory, so we must evaluate the efficiency through numerical methods. In this case, the crystal thickness is fixed to 2 mm and, at the moment, we did searched for an optimized thickness. First of all, we can see that the efficiency can be split in two contributions:

- the diffraction efficiency η_{curv} , which is the ratio between the diffracted and the transmitted intensities without the effect of the self-absorption of the material.
- the self-absorption contribution η_{abs} , which quantifies the fraction of incoming photons that are absorbed by the material and are subtracted from the beam.

The total efficiency can be written as:

$$\eta = \eta_{curv} \cdot \eta_{abs} \quad (2.27)$$

Where the self-absorption term can be written in the well known form:

$$\eta_{abs} = e^{-\mu \frac{T}{\cos \theta_B}} \quad (2.28)$$

Where μ is the linear self-absorption coefficient for the choosen material, T is the thickness of the crystal and θ_B is the Bragg angle of the incoming radiation. To evaluate η_{curv} , we follow the technique described in the paper by Bellucci et al. (2013). First of all, we suppose that the beam impinging on the crystal is monochromatic and arbitrarily narrow. Then we divide the crystal in a series of lamellae, which can be considered as very thin crystals, slightly misaligned between each others. Each lamella has a thickness equal to half the extinction length Λ_0 , which assures us that 96% of the photons of the incoming beam undergoes one single interaction (Authier 2003) while crossing the lamella. Since the lamella is very thin, we can suppose that it is always in the strongly curved regime. A crystal will be composed of an integer number of lamellase N , such that its total thickness is:

$$t = N \frac{\Lambda_0}{2} \quad (2.29)$$

In the case of a perfect cylindrical curvature, the misalignment δ_0 between the two adjacent lamellae is the ratio between the size of a single lamella and the curvature radius of the planes of the crystal R_s :

$$\delta_0 = \frac{\Lambda_0}{2R_s} \quad (2.30)$$

The efficiency profile of a lamella can be written as:

$$f(\theta, R_s) = e^{-(\Delta\theta)^2/(2\sigma^2)} \cdot \left(1 - e^{-\pi^2 d_{hkl} R_s / \Lambda_0^2}\right) \quad (2.31)$$

The first term describes the dependence on the misalignment from the Bragg angle, expressed by the quantity $\Delta\theta$. The quantity σ is linked to the Darwin width of the crystal through the relation:

$$\sigma = \frac{2}{2.35} \delta_W \quad (2.32)$$

The second term in Eq. 2.31 is the diffraction efficiency for a strongly curved crystal. Then we suppose that the beam hits the surface of the crystal at the Bragg angle and that it interacts with the crystal every half extinction length, so at the lower end of each lamella. Each interaction consists in a Bragg's diffraction of the beam and splits the beam in two branches. With this assumption, if we have N lamellae, then we have $n = N - 1$ interactions, so the beam will be split in 2^n branches. Since the crystal is curved, the misalignment between the branches and the diffraction planes changes. We can represent those misalignments (in unit of δ_0) with a matrix of size $[2^n, n]$, where n is the total number of diffractions of the beam. Each row of the matrix represents one of the branches and the columns represents the order of diffraction, where we use the term "order" to indicate the number of time the beam has been split. Each entry of a row represents the misalignment at a given order with respect to the immediately previous order. The matrix, which we call path matrix, has then the following shape:

$$path^{(n)} = \begin{pmatrix} -1 & -1 & -1 & \dots & -1 & -1 & -1 \\ -1 & -1 & -1 & \dots & -1 & -1 & 1 \\ -1 & -1 & -1 & \dots & -1 & 1 & -1 \\ -1 & -1 & -1 & \dots & -1 & 1 & 1 \\ & \vdots & & \vdots & & \vdots & \\ 1 & -1 & -1 & \dots & -1 & -1 & -1 \\ 1 & -1 & -1 & \dots & -1 & -1 & 1 \\ & \vdots & & \vdots & & \vdots & \\ 1 & 1 & 1 & \dots & 1 & 1 & 1 \end{pmatrix} \quad (2.33)$$

For clarity, we show some examples of path matrix for some value of n :

$$path^{(1)} = \begin{pmatrix} -1 \\ 1 \end{pmatrix}; \quad path^{(2)} = \begin{pmatrix} -1 & -1 \\ -1 & 1 \\ 1 & -1 \\ 1 & 1 \end{pmatrix}; \quad path^{(3)} = \begin{pmatrix} -1 & -1 & -1 \\ -1 & -1 & 1 \\ -1 & 1 & -1 \\ 1 & -1 & -1 \\ 1 & -1 & 1 \\ 1 & 1 & -1 \\ 1 & 1 & 1 \end{pmatrix}; \dots$$

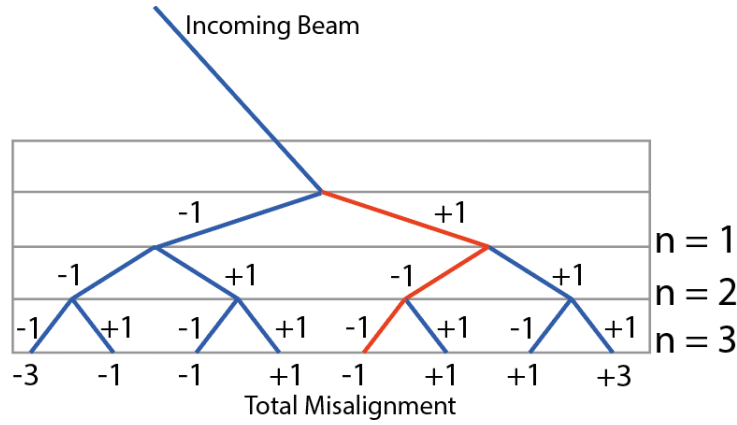


Figure 2.10: Representation of the branching of the incoming beam inside a crystal in the case in which the crystal is divided in four lamellae. The numbers represent the misalignment of every branch with respect to the previous is in fraction of δ_0 . The red branch in figure has a total misalignment of $-\delta_0$ with respect to the incoming beam. The physical angle of diffraction are the same for every branch, but they have been slightly changed in the drawing for clarity.

To show in a more clear way the meaning of the entries of those matrices, we consider an example in the case $n = 3$, which corresponds to a total number of lamellae of $N = 4$. Let us consider the fifth row of the matrix:

$$[1, -1, -1]$$

This means that we are considering the branch that has been diffracted to a direction $+\delta_0$ with respect to the very first lamella, then $-\delta_0$ with the second lamella and finally a misalignment $-\delta_0$ with respect to the third lamella. Its total misalignment with respect to the incoming beam is $+\delta_0 - 2\delta_0 = -\delta_0$. A visual representation of this can be seen in Fig. 2.10, where the path of the red branch is described by the above row of the matrix. As shown by Bellucci et al. (2013), if we ignore self-absorption, the fraction of total photons of the beam flowing in the i^{th} branch at the n^{th} order of diffraction can be expressed as:

$$\begin{aligned} \eta_{i,n} = & \left| \frac{1 - \text{path}_{i,1}^{(n)}}{2} - \exp(-\pi^2 d_{hkl} R / \Lambda_0^2) \right| \times \\ & \times \prod_{j=1}^{n-1} \left| (\text{path}_{i,j}^{(n)} + \text{path}_{i,j+1}^{(n)}) / 2 - \left\{ \exp \left[- \left(\delta_0 \sum_{k=1}^j \text{path}_{i,k}^{(n)} \right)^2 / (2\sigma^2) \right] \right\} \right. \\ & \left. \times [1 - \exp(-\pi^2 d_{hkl} R / \Lambda_0^2)] \right| \quad (2.34) \end{aligned}$$

Then the total efficiency after n interaction is given by the sum of the efficiencies of all the branches oriented in the direction of diffraction:

$$\eta_n = \sum_{i=1}^{2^n} \eta_{i,n} (1 - \text{path}_{i,n}^{(n)})/2 \quad (2.35)$$

The last thing that we must do is to take in account the fact that the crystal is thick and interaction is continuous, so the real point of interaction in a lamella can change randomly. To take this in account, we can evaluate the efficiency as the average of the efficiency with n lamellae and the efficiency with $n + 1$ lamellae. The total efficiency after n diffractions can then be evaluated as:

$$\eta_{n,tot} = \frac{\eta_n + \eta_{n+1}}{2} \quad (2.36)$$

With this algorithm we can evaluate the efficiency of a perfect curved crystal outside the Dynamical theory regime for every possible combination of curvature radius or energy we desire.

2.2.1 Diffraction by higher order planes

For the construction of the ASTENA-NFT, we want to use the (111) planes of the crystals. However we can see that also planes whose Miller indexes are of the type (n, n, n) , with n positive integer, are capable to diffract radiation at the same Bragg's angle of the (111) planes. To see this, we first consider the first diffraction order of Bragg's law for the first planes:

$$2d_{111} \sin \theta_B = \lambda^{(1)} \quad (2.37)$$

where we called $\lambda^{(1)}$ the wavelength of the radiation that satisfies the Bragg's condition. Then we consider the diffraction given by the (n, n, n) planes and we suppose that we don't change the angle:

$$2d_{n,n,n} \sin \theta_B = \lambda^{(n)} \quad (2.38)$$

where $\lambda^{(n)}$ is the wavelength of the radiation the satisfies the Bragg's law for those planes. Since the Bragg's angle is the same, we need to require that:

$$\sin \theta_B = \frac{\lambda^{(1)}}{d_{111}} = \frac{\lambda^{(n)}}{d_{n,n,n}} \quad (2.39)$$

The interplanar distance of the planes can be written as (see Zachariasen):

$$d_{hkl} = \frac{a}{\sqrt{h^2 + k^2 + l^2}} \quad (2.40)$$

where a is the lattice parameter of the unit cell. From this relation, we can notice that:

$$d_{n,n,n} = \frac{d_{111}}{n} \quad (2.41)$$

Inserting this in the relation 2.39 we can write:

$$\lambda^{(n)} = \frac{\lambda^{(1)}}{n} \quad (2.42)$$

which translates in a relation on the energies of the diffracted beams:

$$E^{(n)} = n E^{(1)} \quad (2.43)$$

This means that a crystal fixed to a chosen Bragg's angle, is able to diffract not only the radiation of energy $E^{(1)}$, but also multiples of the same radiation which are diffracted from higher order planes. We can compute the efficiency of diffraction of those planes using the same methodology described in the previous section, with the following corrections:

- We perform the substitution $d_{hkl} \rightarrow d_{hkl}/n$ in every place the interplanar spacing appears.
- We take in account the value of the structure factor F_h for the new planes we are considering.

In a diamond cubic lattice such as the one of Si and Ge, the diffraction from the planes (222) is forbidden, so the first useful planes are the (333), for which the atomic structure factor is smaller than the (111) planes (see Cullity 1978). A smaller structure factor translates in a greater extinction length (Eq. 2.10), which, according to 2.21, results in a lower diffraction efficiency. The planes (444) have an extinction lengths comparable with the (333), however they are associated to even higher energies, so we don't expect that they will give a substantial contribution. The (555) are associated to extinction length way greater than the one for (333) (Fig. 2.11), so we aspect that their contribution to the total efficiency is way smaller. In our estimate of the total efficiency, we decided to add only the contribution of the (333) plans, since we can expect that the contribution of higher order planes is smaller and will not change significantly the total efficiency of the crystal.

2.2.2 Estimated efficiency for the Ge(111) and Si(111) crystals

Applying the algorithm described above, we evaluated the efficiency for the crystals that will be used in the construction of the ASTENA satellite. The energy band for which the computation has been performed are [50 keV - 355 keV] for Si(111), [150 keV - 500 keV] for Si(333), [140 keV - 610 keV] for Ge(111) and [420 keV - 1000 keV] for Ge(333). The results are show in Fig. 2.12 and Fig. 2.13. From this, it is immediately evident that:

1. Silicon is more efficient than Germanium for energy lower than about 150 keV, then their efficiency is comparable in the range 150 keV-180 keV. Above 180 keV, Germanium is always more efficient than Silicon.

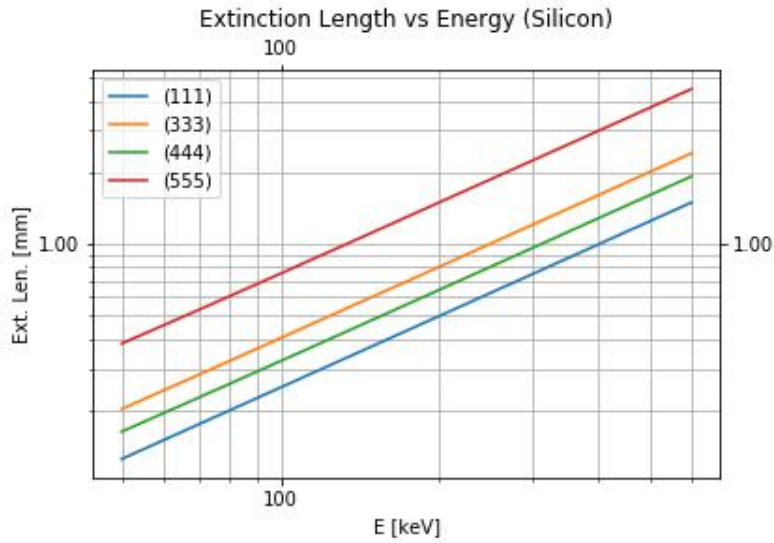


Figure 2.11: Extinction length in crystal of Silicon as function of energy for the families of diffracting planes (111), (333), (444) and (555).

2. The efficiency of the (333) planes is way lower than the efficiency of the (111) planes. The contribution from those planes becomes soon almost negligible, nonetheless there is still a small, useful contribution that increases the total efficiency of a crystal.
3. The expected efficiency for the (444) planes and higher planes is even smaller than the efficiency of the (333). We can safely exclude those planes from this first estimate of the efficiency without committing significant errors.

From those results, we can see that the best way to optimize the performance of lens for the ASTENA-NFT is to use the Silicon on the rings diffracting radiation in the band [50 keV - 170 keV] and Germanium on all the higher energies rings. This means that we can also exploit the efficiency of the Si(333) planes in the band [150-510 keV] and the efficiency of the Ge(333) above. The efficiency obtained in this way will be used to evaluate the total sensitivity and the effective area of the whole lens.

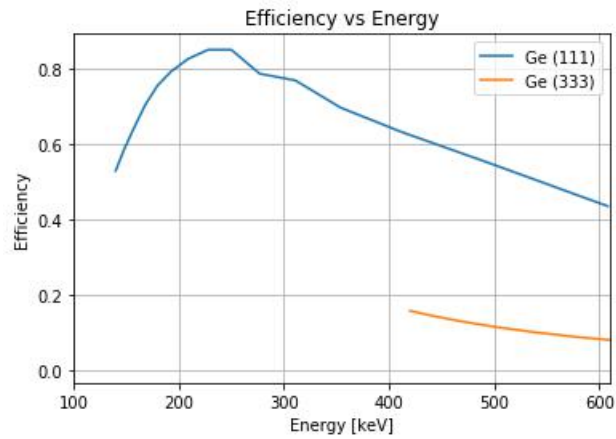


Figure 2.12: Evaluated reflection efficiency as function of energy for a crystal of Germanium. The efficiency for the (111) planes is plotted from 140 keV to 610 keV, while the efficiency for the (333) planes is shown from 420 keV to 610 keV.

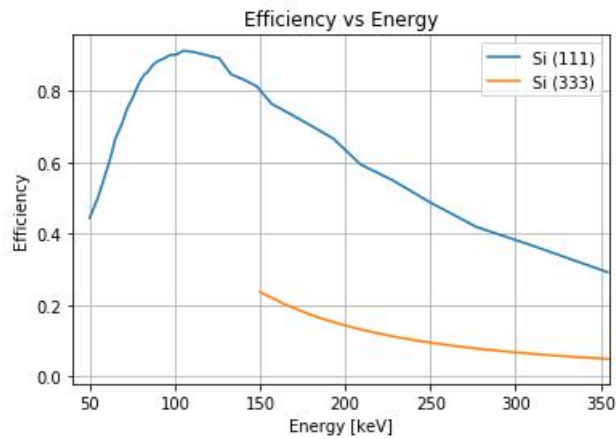


Figure 2.13: Reflection efficiency as a function of energy for a Silicon crystal. The efficiency for the (111) planes is plotted from 50 keV to 355 keV, while the efficiency for the (333) planes is shown from 150 keV to 355 keV.

Chapter 3

Software development and simulations for the optics and the focal plane detector of the NFT

Physical modeling is a fundamental step for the development of every type of instrumentation, including the one aboard ASTENA: the performances of both the Laue lens and the focal plane detector at the basis of ASTENA/NFT need to be studied with simulations. During the course of the previous years, the HE Astrophysics group at the university of Ferrara developed a tool, the Laue Lens Library (LLL), able to simulate a Laue lens and its behaviour with different type of sources. The LLL software is actively used for the simulation of the Point Spread Function (PSF) and for the evaluation of the effective area for the NFT lens. Recently, we decided to further improve this software by writing a Graphical User Interface (GUI), which enables a faster and easier use of the simulation code both by the developers and external users. The focal plane detector, instead, is simulated using the MEGALib software. In this Chapter, we will give a brief description of both software, we will describe the new functionalities of the LLL software and we will present the results of the simulations of the focal plane detector of NFT.

3.1 The "Laue Lens Library" simulation code

The LLL simulation software is a Python software developed by the High Energy Astrophysics group of the University of Ferrara. Over the past year, it has been widely tested and used to simulate Laue lens observations with different configurations and type of crystals (see Virgilli et al. 2017 for an example with bent crystals). Thanks to this software, it is possible to simulate lenses with different configurations (single crystal, circular sector, sin-

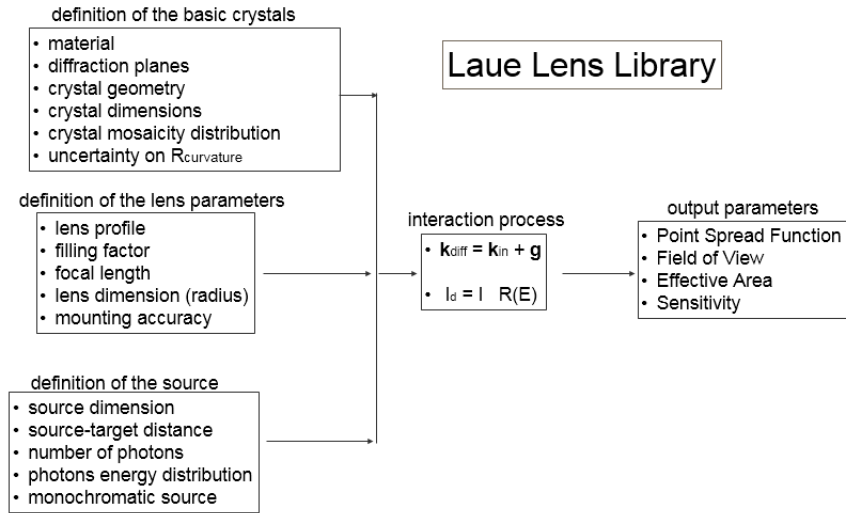


Figure 3.1: Scheme of the libraries used in the LLL software, including relevant input and output parameters.

gle ring of crystals, multiple rings) and constructive properties, such as the focal length or the distance between the various crystal tiles. The four configurations of the lens currently implemented in the software are:

- **Single crystal**, which is a lens made by a single crystal able to diffract a chosen energy.
- **Single ring**, which consists of a circular ring of crystals all diffracting the same energy.
- **Multiple rings**, which consists of a lens made of a series of circular rings able to diffract radiation between the chosen maximum and minimum energies.
- **Sector**, which consists of a circular sector of a multiple rings lens. As in the case of the multiple rings, a sector is able to diffract radiation between a maximum and minimum energy.

The software is able to simulate the behaviour of both perfect and mosaic crystals, with different curvature radius and of different materials, including Silicon and Germanium. The software allows to simulate the presence of mounting misalignment angles and their distribution, the distribution of the curvature radius of the crystals and the distribution of their mosaicities/quasi-mosaicities. Various type of sources can also be simulated. The most important libraries which make up the LLL code are the following (Fig. 3.1):

- **Lenses:** it contains the definition of the geometrical configuration of the lens. Each configuration is described by an appropriate class and contains all the physical and constructive properties of the lens. The definition of the crystals is also contained in this library.
- **Sources:** it defines the type of available sources. The code is able to simulate polychromatic and monochromatic radiation, point-like and extended sources, divergent and divergenceless beams and finite distance or astronomical sources.
- **Detector:** it contains the class and methods which simulate the focal plane detector. The simulated detector works both as an imager and as a spectrograph. It is considered as an ideal detector, i.e. its efficiency is maximum and identical for every energy.
- **Physics:** it contains all the functions which describe the physics of the interaction between the photons and the lens.

With this tool, it is possible to obtain simulations of the PSF of a Laue lens and evaluate the effective area, the field of view and the sensitivity of the system. In earlier versions, the user interface was an input file (*Macro.py*) which needed to be filled with all the structure and input parameters of the lens, the crystals, the source and the detectors. Such a way to manage the input parameters was not very user-friendly and made the tool difficult to use for non-developers. For this reason, we decided to add a true Graphic User Interface (GUI) to our tool.

3.2 GUI programming in Python

Before describing in detail the GUI, we will describe the very basis of GUI programming. GUI programming is said to be "event driven", i.e. based on the handling of the so-called "events".

An event represents an interaction between the GUI and the user, which can vary from simple things such as clicking on a button, or modifying a text field, to more complex interactions. The GUI constantly "listens" for events generated by user interactions and inputs and, when an event is detected, the execution of a series of specific functions is triggered. Those functions take the name of "event handlers" and are executed in a sequential way. Once the execution of those functions is terminated, i. e. the event is successfully handled, the GUI goes back in "listening mode", waiting for new inputs by the user. In this way it is possible to associate the action of the user to the execution of specific instructions. Building the event handling system from scratches, including all the event listening and event generator methods, is a long and complex job and it is usually the work of specialized software engineers.

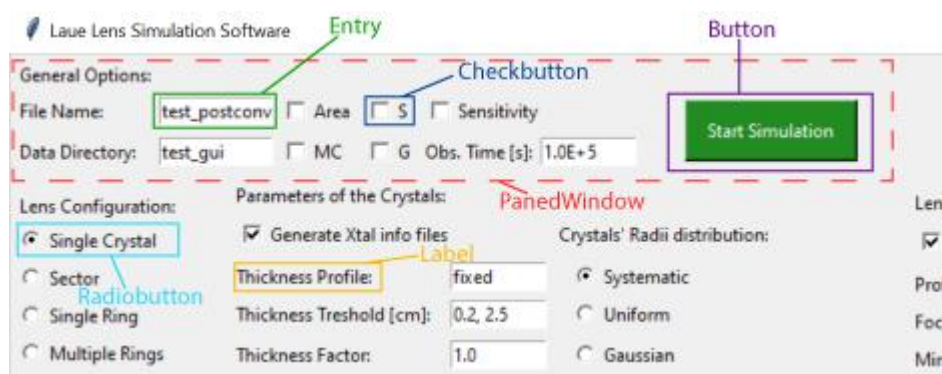


Figure 3.2: Section of the LLL GUI with an example of the type of *Tkinter* widgets used.

However, it is possible to use specific libraries and frameworks, entirely dedicated to GUI programming, which allows non-professional developers to construct full functioning Graphical User Interfaces. The event listening and generation is handled by the built-in classes of the libraries and the work left to the developer is the construction of the GUI and the writing of the event handler functions, which can be associated to various predefined types of events. In this way, the development of a GUI is strongly simplified.

3.2.1 The *Tkinter* library

In Python, one of the most used GUI developing tool is the *Tkinter* library. This pack of libraries contains all the classes and the function which can be used to easily create basic GUIs, so its a good choice for our needs. *Tkinter* is based on *window* objects, which constitute the skeleton of the GUI and are instances of the *Tk* class. On those windows, it is possible to place *widgets*, which are prebuilt objects, such as labels, text box, buttons and many others, that we can use to build the GUI. Each widget is an instance of its specific class, e.g. each label we put on the window will be a separate instance of the *Tkinter*'s class *Label*. For the construction of the GUI, we used the following widgets:

- **PanedWindow:** this widget acts as a "container" of child widgets. It is invisible to the user, but helps the developer to position the various widgets in a easier and tidier way.
- **Label:** this widget consists of a simple text label which cannot be modified by the user.
- **Entry:** it consists of a white text box which can be used both to display outputs and to read user inputs.

- **Button:** this widget is a clickable button. It is possible to associate a Python function to the button: the action of clicking on the button will trigger the execution on the chosen function.
- **Checkbox:** it consists in a small, square button used to display True or False selections. It can be used alone or grouped with other widgets of the same type to represent more complicate selection cases.
- **Radiobutton:** it consists in a circular button which is always associated with other *Radiobuttons* and is used to select an option among multiple choices.

An example of the appearance of those objects is shown in Fig. 3.2.

3.3 The new GUI

To construct the main window of the GUI, we created the class *mainForm*, which contains the definition of the *Tkinter* window object itself, the definition of all of its widgets and support variables and the definition of the event handler functions. The widgets are created and placed on the main window by the user defined function *Builder*, which contains the instructions necessary to create and pack all the widgets. The GUI constructed in this way is show in Fig. 3.3. The various feature of the GUI are grouped in different panels, which we will describe separately.

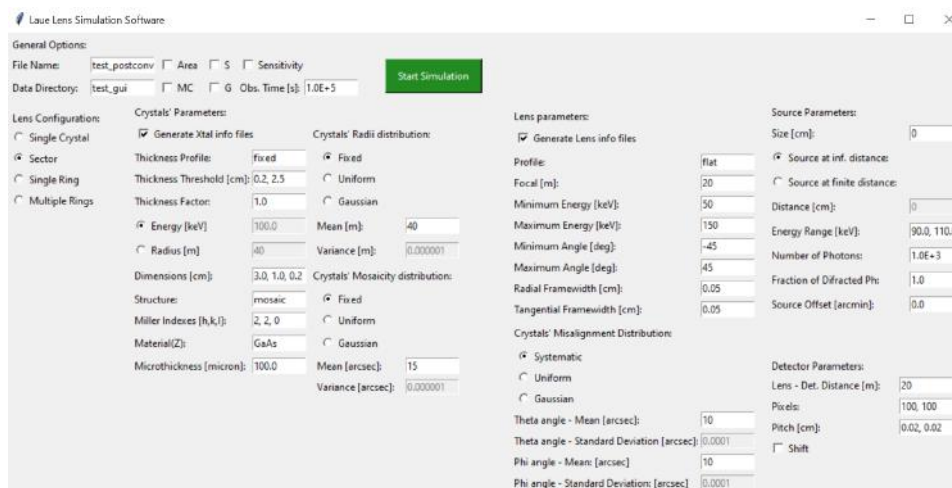


Figure 3.3: The new Graphical User Interface of the *Laue Lens Library* simulation software.

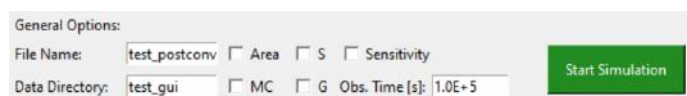


Figure 3.4: The "General Options" panel of the GUI.

3.3.1 "General Options" panel

This panel is shown in detail in Fig. 3.4. Inside the *Entry* widgets in this panel, the user can input the name of the output files and the directory in which they will be saved. The simulated observation time can be inserted in this panel. With the *Checkbuttons*, it is possible to select among various operations which can be performed by the LLL software:

- **Area:** when this option is chosen, the software evaluates the effective area of the lens.
- **MC:** when this option is chosen, the software produces the PSF of the lens through a Monte Carlo simulation.
- **Sensitivity:** when this option is chosen, the software evaluates the sensitivity area of the lens.
- **S:** when this option is chosen, the software evaluates the equivalent area $S(E) = (f(E)A_{\text{eff}})^2 / A_{f(E)}$ which was defined in Eq. 2.8.
- **G:** when this option is chosen, the software evaluates the ratio between the collecting area and the detection area of the lens.

The calculation are launched by pressing the button "Start Simulation". The input values for crystals, lens, source and detector are read from the other panels of the GUI.

3.3.2 "Lens Configuration" panel

The "Lens Configuration" panel allows the user to choose one of the four lens configurations currently available: single crystal, circular sector, single ring and multiple rings. The appearance of this panel is shown in Fig. 3.5



Figure 3.5: The "Lens Configuration" panel of the GUI.

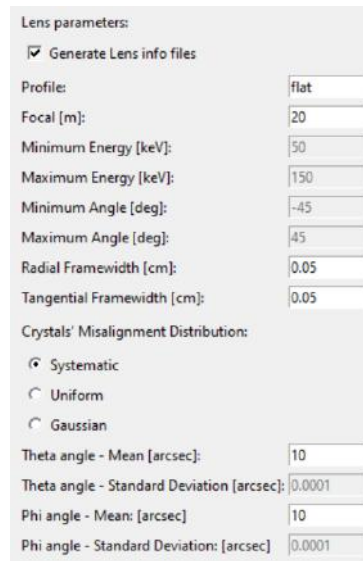
Figure 3.6: The "Crystals' Parameter" panel of the GUI.

3.3.3 "Crystals' Parameters" panel

This panel (shown in Fig. 3.6) allows the input of all the information concerning the crystals, including their sizes, internal structure, the diffracting planes and the material. It is also possible to simulate a distribution of the curvature radius and of the mosaicity/quasi-mosaicity of the crystals. The simulation of the mosaicity distribution, in particular, has been added along with the GUI upgrade. For both curvature radius The available options are a "Fixed" value, an "Uniform" distribution and a "Gaussian" distribution. The "Energy/Radius" selection is used only in the case of a single crystal or single ring lens and they both define the energy diffracted by the lens, either with the direct input in the "Energy" field, or with the input of the distance from the center of the lens in the "Radius" field.

3.3.4 "Lens Parameters" panel

This panel (shown in Fig. 3.7) allows one to enter all the information concerning the whole structure of the lens. With this panel, it is possible to choose the profile of the lens, its focal distance and the frame width between crystals. The minimum and the maximum energy fields are used in the "sector" and "multiple rings" configuration, while the minimum and maximum angle are used only in the case of a lens in sector configuration and define the shape of the sector. It is possible to choose a distribution for the mounting misalignment angles θ and ϕ of the crystals. The angle θ represents a misalignment on the Bragg's angle, while the angle ϕ represent a



Lens parameters:

Generate Lens info files

Profile: flat

Focal [m]: 20

Minimum Energy [keV]: 50

Maximum Energy [keV]: 150

Minimum Angle [deg]: -45

Maximum Angle [deg]: 45

Radial Framewidth [cm]: 0.05

Tangential Framewidth [cm]: 0.05

Crystals' Misalignment Distribution:

Systematic

Uniform

Gaussian

Theta angle - Mean [arcsec]: 10

Theta angle - Standard Deviation [arcsec]: 0.0001

Phi angle - Mean [arcsec]: 10

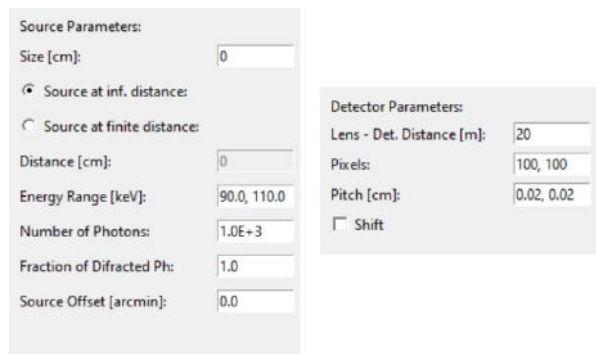
Phi angle - Standard Deviation [arcsec]: 0.0001

Figure 3.7: The "Lens Parameters" panel of the GUI.

rotation of the crystal on the plane of the lens. It is possible to choose between a systematic mounting error, an uniform distribution or a Gaussian distribution of the error.

3.3.5 "Source Parameters" and "Detector Parameters" panels

Those panels (in Fig. 3.8) allow one to define the type of source and the characteristics of the detector. It is possible to select the size of the source, the distance from the lens, the energy range in which the source emits, the fraction of photons diffracted and, finally, the off-axis angle of the source ("Source Offset"). The "Number of Photons" represents the number of photons which are simulated in the Monte Carlo process. In the detector panel,



Source Parameters:

Size [cm]: 0

Source at inf. distance:

Source at finite distance:

Distance [cm]: 0

Energy Range [keV]: 90.0, 110.0

Number of Photons: 1.0E+3

Fraction of Diffracted Ph: 1.0

Source Offset [arcmin]: 0.0

Detector Parameters:

Lens - Det. Distance [m]: 20

Pixels: 100, 100

Pitch [cm]: 0.02, 0.02

Shift

Figure 3.8: The "Source Parameters" panel of the GUI.

it is possible to choose the distance between the detector and the lens, the number of pixels on the detector and their pitch. The *Shift* option can be used to automatically adjust the distance between lens and detector in a way that the image is always captured on focus.

3.4 Simulations of the focal plane detector of the NFT

The NFT is composed by two decoupled elements which are the Laue lens optics and a focal plane detector. While the first is the responsible for the collecting area of the instrument, the second is the responsible for the detection of the photons that are collected by the lens. Even though for the optimization of the instrument the focal plane detector has to be defined on the basis of the lens throughput, the two devices work in a completely disjoint manner. In this Section I will focus on the simulation of a suitable focal plane detector which is optimized in terms of efficiency, energy pass-band and pixel size with respect to the Laue lens best achievable performances.

3.4.1 The MEGALib software

The Medium-Energy Gamma-ray Astronomy library (MEGALib) is a set of software tools designed to simulate and analyze the performances of X and γ -ray telescopes. The software is written in C++ and is based on ROOT and Geant4: the first is a framework for data processing, born at CERN for high energy physics, the second is a toolkit for the simulation of the passage of particles through matter extensively used in high energy, nuclear and accelerator physics (Zoglauer et al. 2006). One of the main feature of Geant4 is its use as geometry modeler thanks to a variety of tools available to recreate the geometry of complex detectors.

MEGALib exploit Geant4 (and in some sense simplify its use) by using optimized algorithms and replicating patterns as high energy detectors are frequently composed by many replicated parts like layers of thin materials. Thick layers of materials would increase the probability of interaction of the radiation within the volume of the detector, however they are not technologically available, therefore we need to use thinner layers. As Geant4, MEGALib adopt the philosophy of the definition of the volumes as geometrical elements, of the materials of which each part is made and if each volume represents an active part (detection volume), a passive material (pure absorbing volume) or an active shield (Veto). It is also possible to create volume made of a given composition of elements (for example Cadmium Zinc Telluride detector).

Another important feature of Geant4 is the possibility to simulate the generation of a flux of photons or particles and to evaluate the full interaction of them with the detector, including the generation of secondary

particles and radiation. The MEGAlib software is able to generate the entire data analysis chain and has been used in different mission design for detector calibration, evaluation of the effects of surrounding passive materials and other scientific instruments (all representing passive elements for the instrument of interest on board a satellite), reconstruction of the arrival direction of the radiation by exploiting the Compton and pair production kinematics and for a number of high level data analysis such as polarization analysis and sensitivity calculation.

In this Section, simulated data concerning the focal plane detector are presented. Nevertheless, experimental results have been taken from the literature. For instance the energy resolution of the detector has been obtained from Kuvvetli (2003) and the results have been used in the Monte Carlo.

3.4.2 Detector geometry

Being 600 keV the upper limit of the NFT energy pass-band, an high Z solid state detector must be used in order to achieve good resolution and efficiency at that energy, which is the most critical for the high probability of Compton interaction and subsequent escape of secondary photons from the detector. The material chosen for the detector active area is Cadmium Zinc Telluride (CZT), which in the last decades has shown to be an excellent compromise between performances and ease of use in space, due to possible employ at room temperature without the requirement of cooling, which is quite demanding in space.

The dimensions of the focal plane detector required for the NFT depends on different factors. With reference to Fig.3.9, the x-y plane corresponds to the plane perpendicular to the focal axis which is the z axis. As the PSF spreads with increasing of the off-axis angle, the dimensions in the x and y coordinates are related to the field of view of the instrument. Considering a FoV of few arcminutes, the dimension of $10 \times 10 \text{ cm}^2$ is a good trade off between a required focal plane extension and the reduced size, limiting the weight and the background. The thickness of the detector (in the z direction) depends on the required efficiency of the focal plane detector. If more than 80% of the photons need to be stopped in the active area, an equivalent thickness of the detector of 10 cm must be accommodated. Unfortunately, the present technology does not allow such a thick crystal to be realized. Nevertheless, it is possible to produce slices of crystals with a thickness of the order of 0.5 cm, therefore we have simulated 20 layers of CZT. In order to make the simulation more realistic, we assumed that each CZT layer lays over a printed circuit board (PCB) 1 mm thick, which acts as support and gives a certain amount of absorption. Each layer of active detector made of CZT has been simulated using the voxel MEGAlib class, which represents the extension of the concept of pixel in three dimensions.

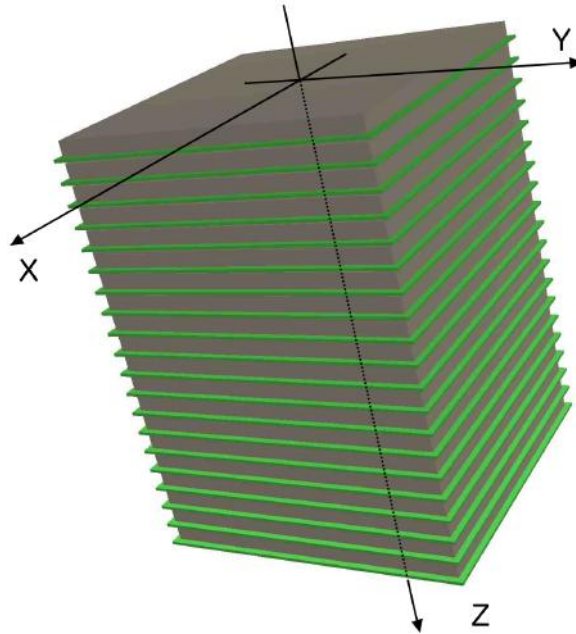


Figure 3.9: A 3D view of the designed NFT focal plane detector made with MEGAlib.

The spatial resolution has been chosen of $250 \mu\text{m}$ in all the three directions.

Despite the excellent energy resolution of Silicon and Germanium detectors, their low stopping power for high energy photons limits their application to hard X-rays. On the other hand, Cadmium Zinc Telluride and Cadmium Telluride (CdTe) have lower energy resolution but with the remarkable advantage of the possible use at room temperature. In Fig. 3.10 is shown the measured energy resolution for CZT detector as a function of energy. As can be observed, from tens to hundreds of keV (even outside the energy pass band of our interest) the energy resolution correlate with the energy. A linear fit has been done and the parameters have been used in our simulation ($m = 0.0044$, $q = 0.92$).

3.4.3 Detector performances estimation

MEGAlib has been conceived for Compton and pair production imaging, i.e. for exploiting the Compton interaction, the e^+/e^- production and their kinematics for the reconstruction of the direction of the incoming photons. Such instruments are direct view detectors, without a focusing optics in which the source flux uniformly illuminate the detector from a "far field". Nevertheless, this tool can be exploited, with some artifice, for the design and optimization of the focal plane detector of focusing instruments. In

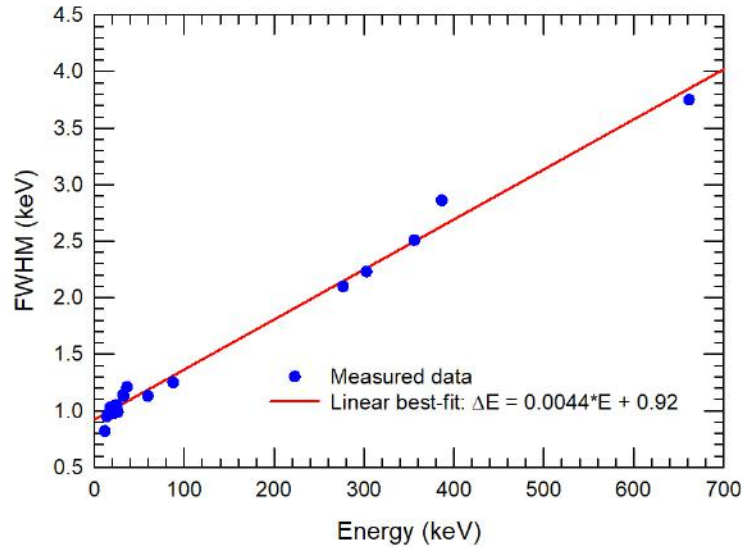


Figure 3.10: Experimentally measured energy resolution for a CZT based detector as function of energy. The red line is the linear best fit. The best fit parameters have been used in our software to take into account the energy resolution of a CZT based focal plane detector. Reprinted from Kuvvetli (2003).

order to evaluate the detector performances, we have simulated the flux incoming on it from the Laue lens optics, 20 m far on the top of the detector. The main differences with respect to the direct view Compton imaging can be summarized as follows:

- for the detector, the source of radiation is not the far field astronomical source but is the Laue lens itself.
- the detector is not fully illuminated but, instead, the X-ray radiation hits a part of it, depending on the focusing capability of the Laue lens over the focal plane detector.

The previous statements suggest to generate a "near field" source with the following properties and simplifications:

- the simulated source is a disk generated 20 m on the top of the detector with diameter equal to the Half Power Diameter (HPD) of the Laue lens of 1.5 mm.
- the radiation hits perpendicularly to the plane of the detector.

The above assumptions can be accepted in first approximation by taking into account that for a perfect alignment of the crystals, their

overall signal on the focal plane detector surface has a radial profile quasi-gaussian with HPD ~ 1.5 mm. The assumption of using a circular shape beam impinging perpendicularly to the focal plane surface is also acceptable given that the diffraction angles are the order of few degrees, therefore the inclination of the impinging radiation is at most few degrees for the larger radius, which corresponds to the lower energy limit.

3.4.4 Detector spectral response

In this thesis, we discuss only the spectral performances of the NFT. The imaging and polarization performances will be faced afterward. The spectral performances can be evaluated by simulating how effective the instrument would be, observing a well known source for a given integration time. This can be done by using the software XSPEC which is largely used by the X-/ γ -ray community both for real data analysis aimed to model the spectrum of astrophysical sources, both for simulations of instrument performances. For this second approach, three components are required and in the following sections they will be described and discussed. The first component is the redistribution matrix file, which describes how the detector spreads a monochromatic energy into its spectroscopic channels. Then, the ancillary file contains the information of the effective area, as a function of energy, that contributes to the photon collection. Lastly, a background file will be added to the source signal. The background depends on both the satellite orbit and its physical properties.

The redistribution matrix file, RMF

The redistribution matrix (RMF) file represents how the detector distribute a monochromatic signal into its spectral channels. To realize the RMF, a Monte Carlo simulations has been performed for each monochromatic energy in the full instrument pass-band 50 – 600 keV at step of 1 keV. The Monte Carlo takes into account all the possible interactions and the respective cross section. In Fig. 3.11, we show the redistribution of three monochromatic energies (60, 300, 600 keV) within the 512 energy channels of the detector. The redistribution matrix is then in general an asymmetric $N \times M$ matrix with N row corresponding to the number of monochromatic energies which have been simulated and M columns representing the number of energy channels of the detector. For an ideal detector the redistribution matrix has a diagonal shape, instead in the case of a real detector off-diagonal contributions are present.

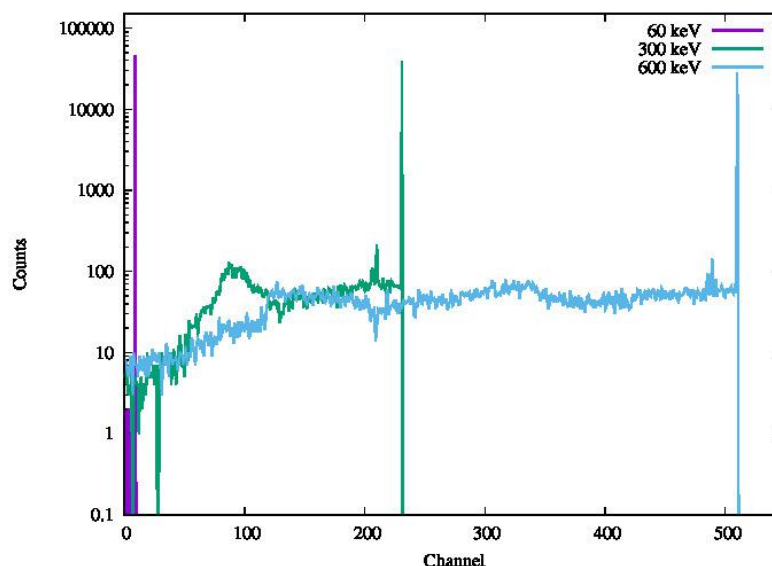


Figure 3.11: Simulations of the redistribution profile for three monochromatic energies: 60 keV (purple curve), 300 keV (green curve), 600 keV (blue curve). The photopeaks corresponding to each respective energy are evident and dominate the spectrum. Nevertheless Compton events and photons escaped from the detector are present and contribute to off diagonal shape of the redistribution matrix.

It is worth mentioning that in Fig. 3.11 the number of photons that interact via photoelectric effect or through Compton scattering are represented, while the RMF y-axis is normalized to the total simulated photons, which is 50000 for each monochromatic energy. The above information are formatted into a fits file with two extension: the first contain the matrix and the second provide the relation between the i -th channel and its lower and upper energy threshold. In Fig. 3.12, we show the structure of the two extensions of the RMF fits file.

The ancillary response file, ARF

In general the response of a detector to a source of photons depends not only on the redistribution of the photons, but also on the sensitivity of the detector to photons of known energy, which is directly related to the effective area of the instrument. For a focusing instrument, the effective area as function of the energy must be explicitly

The figure shows two screenshots of a software interface displaying RMF fits file structure. The top window shows a table with columns ENERG_LO, ENERG_HI, N_GRP, F_CHAN, N_CHAN, and MATRDX. The bottom window shows a table with columns CHANNEL, E_MIN, and E_MAX.

Select	ENERG_LO	ENERG_HI	N_GRP	F_CHAN	N_CHAN	MATRDX
All	keV	keV				285E
1	5.000000E+01	5.100000E+01	1	1	285	Plot
2	5.100000E+01	5.200000E+01	1	1	285	Plot
3	5.200000E+01	5.300000E+01	1	1	285	Plot
4	5.300000E+01	5.400000E+01	1	1	285	Plot
5	5.400000E+01	5.500000E+01	1	1	285	Plot
6	5.500000E+01	5.600000E+01	1	1	285	Plot
7	5.600000E+01	5.700000E+01	1	1	285	Plot
8	5.700000E+01	5.800000E+01	1	1	285	Plot
9	5.800000E+01	5.900000E+01	1	1	285	Plot
10	5.900000E+01	6.000000E+01	1	1	285	Plot

Select	CHANNEL	E_MIN	E_MAX
All	J	keV	keV
1	0	4.000000E+01	4.200000E+01
2	1	4.200000E+01	4.400000E+01
3	2	4.400000E+01	4.600000E+01
4	3	4.600000E+01	4.800000E+01
5	4	4.800000E+01	5.000000E+01
6	5	5.000000E+01	5.200000E+01
7	6	5.200000E+01	5.400000E+01
8	7	5.400000E+01	5.600000E+01
9	8	5.600000E+01	5.800000E+01
10	9	5.800000E+01	6.000000E+01

Figure 3.12: The RMF fits file structure containing the information of the redistribution matrix. *Top*: the first extension where the redistribution matrix is stored (matrix column in which only the first element for each row is visible). Only 10 rows out of 550 are shown. *Bottom*: the second extension stores the *Ebound* (energy bounds) information describing the relation between channels and lower and upper energy threshold for each channel. Only 10 rows out of 512 are shown.

provided. This information must be stored in the so-called ARF file. The ARF usually includes the dependence of the effective area from the off-axis angle of the observed source. Nevertheless, for the time being we have limited our study to on-axis sources. The effective area for the NFT with energy bins of 1 keV is shown in Fig. 3.13. We note that the effective area presents two "jumps": the first jump is at 150 keV and comes from the fact that the (333) planes of Silicon start to contribute to the diffraction, the second jump is at 510 keV and comes from the contribution of the (333) planes of Germanium.

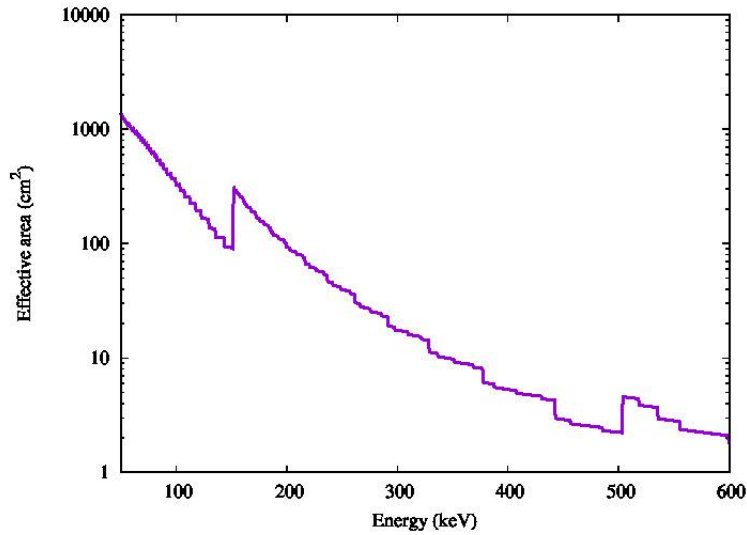


Figure 3.13: The effective area binned at 1 keV for the NFT. The jump in the effective area at 150 keV comes from the contribution of the Si(333) planes, while the jump at 510 keV comes from the effect of the Ge(333) planes.

The background file, BKG

A background file is also required for the evaluation of the NFT performances. The background level was extrapolated to Low Earth

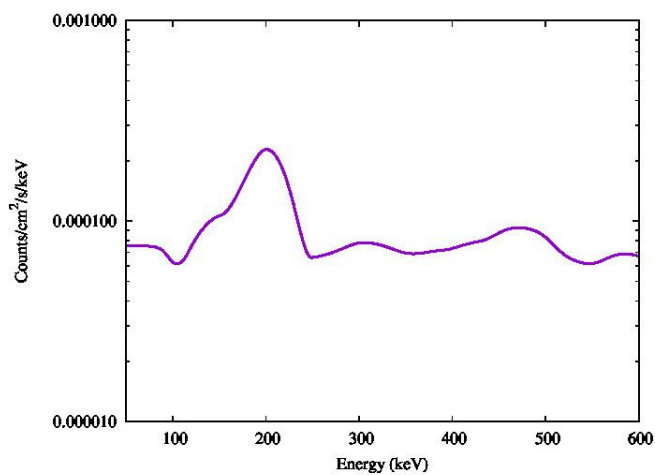


Figure 3.14: The background level for ASTENA. This was extrapolated to Low Earth Orbit (LEO), foreseen for ASTENA, from the measurements of INTEGRAL/SPI operating in a high Earth orbit.

Orbit (LEO) from the background measured with the Spectrometer aboard INTEGRAL (SPI), which is operative in a High Earth Orbit (Virgili et al., 2017), and is shown in Fig. 3.14.

First example of simulated performances: Crab spectrum

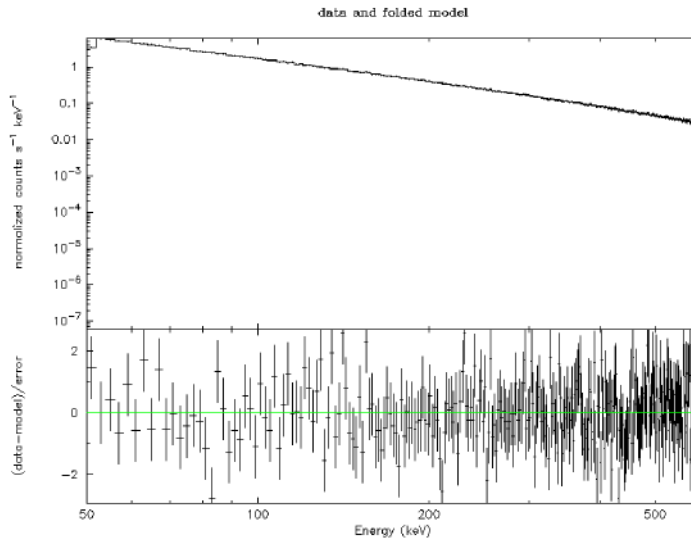


Figure 3.15: Spectrum of the Crab as it would be observed in the energy range 50-600 keV with ASTENA/NFT, with 3000 s integration time. The model is a photoelectrically absorbed power law. The lower panel shows the residuals between data and model in units of sigma.

To obtain a first example of simulated performances for NFT, we used the response matrix, the ancillary file and the estimated background to show how the NFT would observe the Crab with an integration time of 3000s. For this purpose the software XSPEC can be used through the *fakeit* command that allows to generate a simulated spectrum starting from the above files and from the well known typical spectrum of the Crab, which is an absorbed powerlaw. In XSPEC such model is obtained by using the WABS components which simulate a photo-electric absorption using Wisconsin Morrison and McCammon (1983) cross-sections, where σ is the photoelectric cross-section and μ is the equivalent hydrogen column (in units of 10^{22} atoms/cm²), multiplied by a POWER-LAW component $I(E) = k \times E^\alpha$, where α is the photon index of power law and K is the power-law normalization expressed in photons/keV/cm² /s at 1 keV. The parameters of the model for Crab have been taken from the literature (Kuulkers et al. 2003): $\mu = 0.3 \times 10^{22}$, α index = 2.1 and normalization $k=9.7$. The

simulated spectra is shown in Fig. 3.15.

Chapter 4

Future prospects: double diffraction technique

A Laue Lens such as the ASTENA/NFT is based on a single diffraction in Laue configuration and the vast increase in sensitivity afforded by Laue lenses will be a revolution in the field of HE observations. However, Laue lens suffers from aberrations for off-axis sources, which limits their application to narrow field observations. To overcome this limit, new concepts and geometrical configurations of Laue lenses need to be explored. In collaboration with personnel from INAF of the Brera Astronomical Observatory (OAB), we investigated the feasibility of a coupling of crystals in transmission configuration, thus obtaining an high energy analogue of a Kirkpatrick-Baez mirrors system. In this Chapter, we will revise the concept of Kirkpatrick-Baez mirrors and show how we can extend this concept to the case of a Laue lens based on double diffraction coupled crystals in transmission configuration. We will describe the first experimental results of this new configuration and we will suggest how this technique, once mature enough, could be applied to obtain direct hard X-ray images.

4.1 Grazing incidence reflection and Kirkpatrick-Baez mirrors

Kirkpatrick-Baez mirrors are based on the X-ray reflection for grazing incidence angle, hence they can be used for soft X-rays (energies lower than ~ 30 keV) (Kirkpatrick and Baez 1948). Total reflection for grazing incidence is derived from the Snell's law of refraction for electromagnetic waves. Snell's law describes the behaviour of an electromagnetic field at the boundary surface between two different materials and is formulated as:

$$n_i \sin \theta_i = n_t \sin \theta_t \quad (4.1)$$

Where n_i and n_t are the refraction index of the two materials, θ_i is the angle between the propagation direction of the incoming radiation and the normal to the surface and, finally, θ_t is the angle between the transmitted radiation and the normal to the surface. Total reflection happens when $\theta_t = \pi/2$, hence, if the radiation is coming from the vacuum, the condition for total reflection is:

$$\sin \theta_i = n_t \quad (4.2)$$

The crucial point is that X-rays are subjected to anomalous dispersion, i.e. the measured refraction index for X-ray radiation is smaller than 1, which translates in a very small angle θ_i able to produce total reflection. We can define the grazing angle as:

$$\alpha_i = \pi/2 - \theta_i \quad (4.3)$$

Such that:

$$\cos \alpha_i = n_t = 1 - \delta \quad (4.4)$$

Where δ is a real number smaller than one. For small angles, we can expand the cosine at second order, obtaining the relation:

$$\alpha_i = \sqrt{2\delta} \quad (4.5)$$

In the case of materials with high atomic number, the above relation can be written as:

$$\alpha_i \sim 5.6\lambda\sqrt{\rho} \quad (4.6)$$

Where λ is the wavelength of the radiation and ρ is the density of the material. Denser materials and longer wavelengths give higher grazing angles,

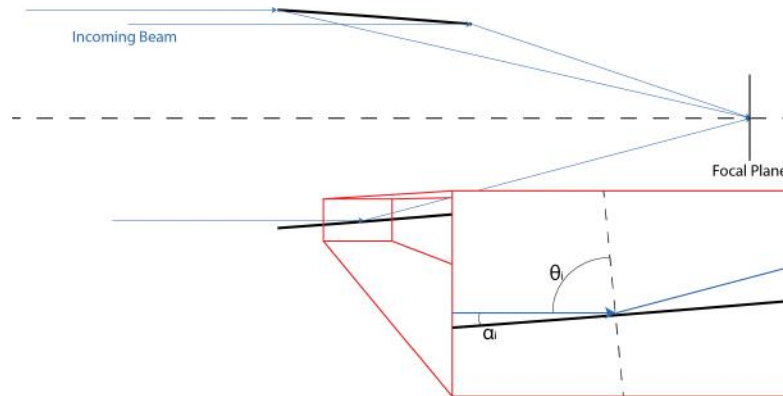


Figure 4.1: Example of a parabolic X-ray mirror based on the grazing incidence technique.

4.1. GRAZING INCIDENCE REFLECTION AND KIRKPATRICK-BAEZ MIRRORS 57

e.g. in the case of Gold and 1 keV photons, the grazing angle is of the order of a few degrees and it rapidly drops below some fractions of degree for energies above 30 keV. Exploiting this reflection, it is possible to deviate and focus X-rays (Fig. 4.1), however the use is limited to low energy X-rays: the grazing angle becomes soon too small and the construction of suitable mirrors becomes impossible.

There are various possible configuration of mirrors which can be used to focus the radiation; one of the most used is the so-called Wolter I configuration, which consist in a combination of an hyperbolic mirror with a parabolic mirror (Wolter 1952). At the moment, the grazing incidence technique has been successfully used in important high energy space missions, such as Chandra X-Ray Observatory and XMM-Newton, which are based on Wolter I optics.

Kirkpatrick-Baez telescopes are based on another configuration of grazing incidence mirrors proposed by P. Kirkpatrick and A. V. Baez in 1948. Those telescopes are made by two subsequent parabolic mirrors whose axis are perpendicular between each others. The first mirror focuses the radiation on a line, then the focused radiation hits the second mirror and is finally focused on a point (Fig. 4.2). Kirkpatrick-Baez telescopes allow one to obtain a direct image of X-ray radiation with a low chromatic aberration, however, their energy range of applicability is very small, since they are based on grazing incidence.

Today's limit for grazing incidence observations was set at 80 keV by the mission NuSTAR (Harrison et al. 2013). To focus higher energies, it is necessary to switch to instruments based on Bragg's diffraction.

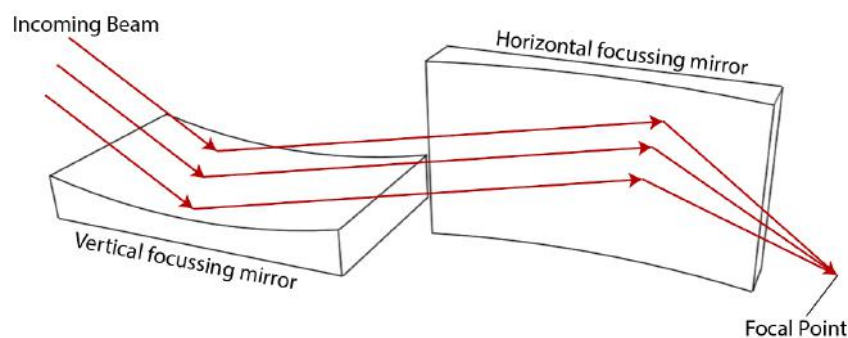


Figure 4.2: Representation of Kirkpatrick-Baez mirrors. The first mirror focuses the radiation in the vertical direction, while the second focuses the radiation in the horizontal direction. The result is that the radiation is focused on a point.

4.2 Double Bragg's Diffraction in Laue configuration

Bragg's diffraction is necessary to focusing hard X/soft Gamma-Rays. Laue lenses, however, show a huge limitation: they suffer for a strong coma-like distortion, which significantly worsen the performance of Laue lenses for off-axis sources (Fig. 4.3). To overcome this limitation it is necessary to imagine new configurations of Laue lenses, so we decided to investigate the possibility of coupling two crystals together in an analogue of a high energy Kirkpatrick-Baez system, but based on X-ray diffraction instead of grazing incidence reflection.

The key idea is to couple two cylindrical curved crystals in a way that the diffraction planes are perpendicular between each others. In this way the beam is first focused along one direction by the first crystal, then it is focused along the other direction by the second crystal. To have a feeling of how this configuration works, we start by imagining that crystals can be divided in a series of thin strips along the direction of the diffracting planes. Since the crystal is curved, each strip focus the radiation and is active to a different, limited energy band.

When a polychromatic beam hits the crystal, each strip will diffract a different range of energies, so we can imagine that the total beam is divided in a series of "sub-beams" with distinct energy bands, which have been focused along one direction. Each one of those sub-beams will then hit the

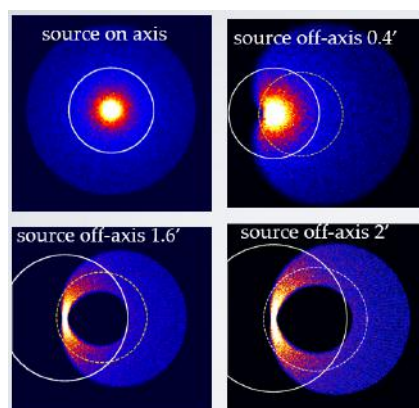


Figure 4.3: Simulation of the PSF of a single diffraction Laue lens made by 10 rings of perfect, bent crystals for various off-axis sources. The energy band of the lens is 200 - 400 keV. The effect of the comatic aberration is evident even for small off-axis angles. The white circle represent the PSF area, centered on the centroid of the distribution, in which 50% of the photons are found. The dashed circle is the optimized circle in which 50% of the photons are found, without the constraint that the circle must be centered on the peak of PSF.

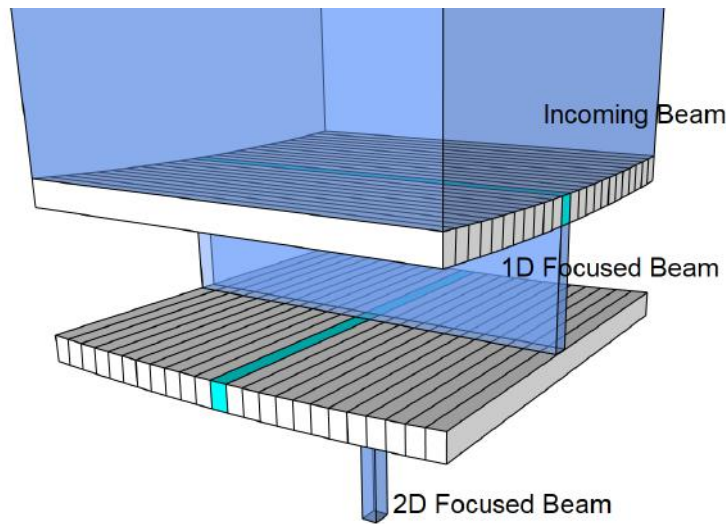


Figure 4.4: 3D representation of a system of two curved crystals coupled. The beam impinging on the whole crystal is first focused by the upper crystal, then the lower crystal further diffracts the beam. At the end, the beam is focused on both directions.

second crystal, whose diffraction planes are orthogonal to the first, in such a way that a piece of all the strips in which it is divided will be "illuminated" by the beam (Fig. 4.4), however only in one of those strips the diffraction planes will be oriented at the right Bragg's angle. The part of the beam which falls in the intersection between the upper strip and the lower strip undergoes two diffractions and is effectively focused on both the vertical and the horizontal direction.

In analogy with the Kirkpatrick-Baez configuration, we don't expect that the focal length of the coupled crystals changes with respect to the focal length of the single crystals, since the two diffractions operate on independent planes. The position of the focus on the focal plane instead is changed with respect to the single diffraction case (Fig. 4.5). To determine the position of the new focal point, we define a reference system in which z is defined by the direction of the incoming photon, x by the non-focussing direction of the first crystal and y by their vector product. We suppose that the wave vector of the incoming beam is completely directed on the z -axis and that the diffracting planes of the first crystal are directed with the x -axis. We can write the wave vector as $\vec{k} = (0, 0, -k)$, where the minus sign indicates that the beam is "falling" toward the lens. The well-known result of this first diffraction is that the beam is rotated on the z - y plane by an angle equal to two times the Bragg's angle, so the wave vector after the first

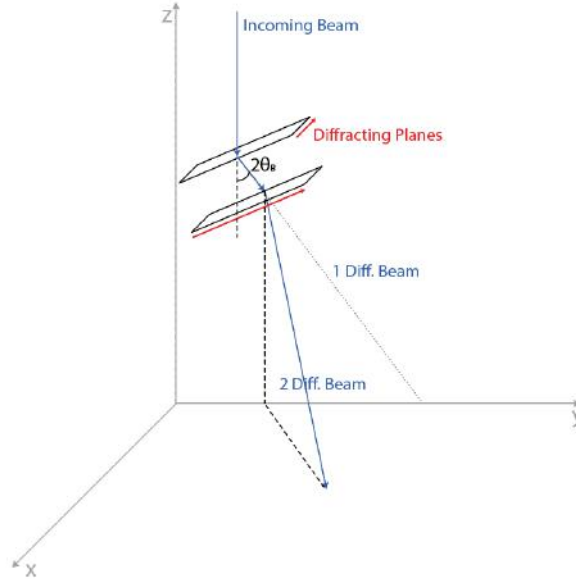


Figure 4.5: The effect of two diffractions on the direction of the beam. The first diffraction rotates the beam on the z - y plane by an angle of two times the Bragg's angle. The second diffraction rotates the beam on the z - x plane.

diffraction will be:

$$\vec{k}_1 = (0, k \sin(2\theta_B), k \cos(2\theta_B)) \quad (4.7)$$

The planes of the second crystal are instead orthogonal to the planes of the first, so the interaction between the 1-time diffracted beam and the second crystal will result in a further redirection of the beam, which is now rotated on the x - z plane (see Fig. 4.5). The final wave vector will be expressed as:

$$\begin{aligned} \vec{k}_2 &= (k_{1,z} \sin(2\theta_B), k \sin(2\theta_B), k_{1,z} \cos(2\theta_B)) = \\ &= (k \cos(2\theta_B) \sin(2\theta_B), k \sin(2\theta_B), k \cos(2\theta_B) \cos(2\theta_B)) \end{aligned} \quad (4.8)$$

To find the position of the new focal point, we evaluate the azimuthal angle ϕ of the vector \vec{k}_2 :

$$\phi = \arctan\left(\frac{k_{2,y}}{k_{2,x}}\right) \quad (4.9)$$

By substituting the expression for the component of \vec{k}_2 in the equation for ϕ , we find:

$$\phi = \arctan\left(\frac{k \sin(2\theta_B)}{k \cos(2\theta_B) \sin(2\theta_B)}\right) = \arctan\left(\frac{1}{\cos(2\theta_B)}\right) \quad (4.10)$$

4.2. DOUBLE BRAGG'S DIFFRACTION IN LAUE CONFIGURATION 61

In the case of small Bragg's angles, we can approximate $\cos(2\theta_B) \approx 1$, which means that:

$$\phi \approx \arctan 1 \approx 45^\circ \quad (4.11)$$

As shown in Fig.4.5, in the case of a single diffraction, the focal point would have been situated on the y-axis of the reference system defined, so the new focal point is rotated by an angle of 45° with respect to the single diffraction focal point. It is important to take in account this redirection when we want to determine where we must position the detector to catch the beam. The change of the focal point is useful because it allows us to ignore the background generated by the presence of the residues 1-D interactions, which we expect that will be too out of focus and far away to increase in a significant way the noise around the double diffracted image.

The analogy with Kirkpatrick-Baez telescope is evident, since the two crystals act as vertical and horizontal "focusers", allowing to squeeze the incoming beam in a focal point, in a similar fashion to what grazing angle mirrors can do to a low energy radiation. It is important however to remark the fact that the underlying physics is completely different, since grazing angle incidence is based on X-ray reflection, while in our case we exploit Bragg's diffraction.

To test the properties and the expected performance of this system, we decided to simulate a ring of coupled crystals. The simulated crystals are mosaic, bent crystals with a cross section of $10 \times 10 \text{ mm}^2$ and a mosaicity

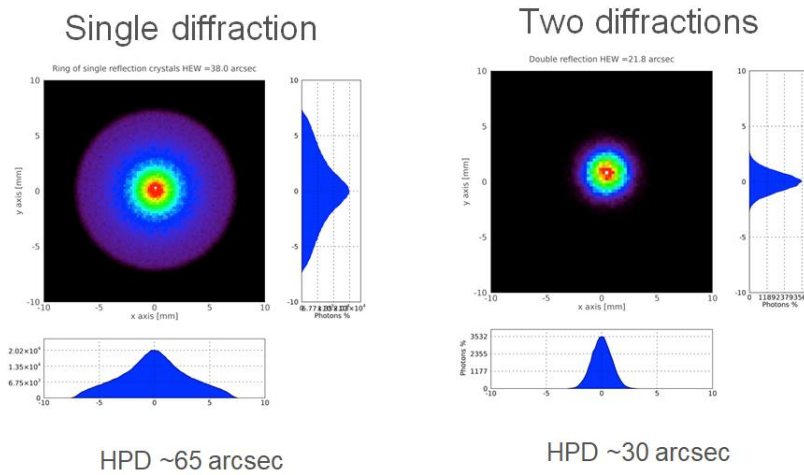


Figure 4.6: Comparison of the Point Spread Function of a ring of single crystals (left) vs a ring of coupled crystals (right). The simulated crystals are bent mosaic crystals with a mosaicity of 15 arcsec and the focal length is 15 m. The improvement in image quality in the case of coupled crystals is evident.

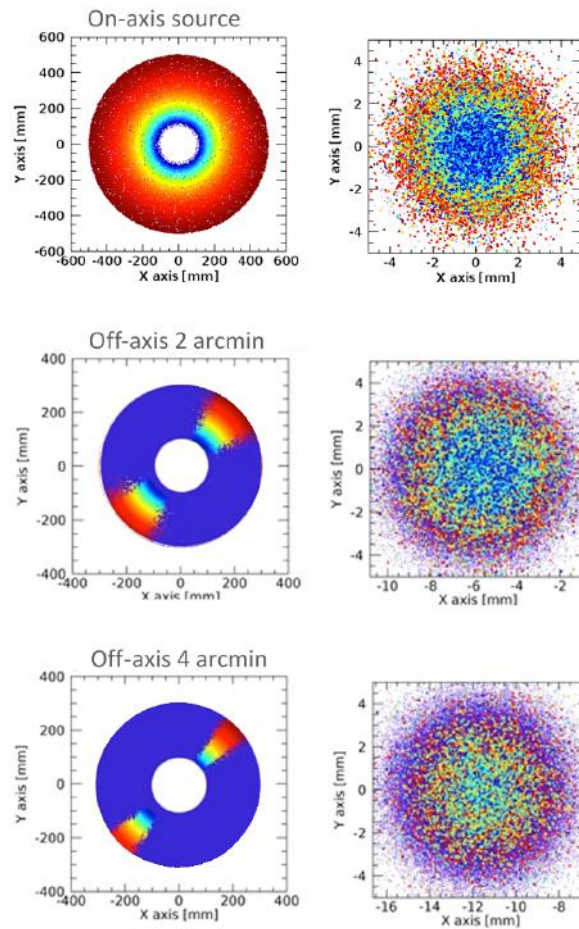


Figure 4.7: Simulations of the behaviour of a double diffraction Laue lens in the case of an on-axis source and two different off-axis sources. The simulated on-axis energy band is 200 – 600 keV. The left plots show the area of the lens which is active in the various cases, with the color encoding the photon energy from low (200 keV, red) to high (600 keV, blue). The right plots are the corresponding Point Spread Functions, with the ray-tracing of photons of different energies (color). The focal length is 15 m. We can see that the active area decreases as the off-axis angle increases, while the PSF is not significantly changed. Note that the dark violet color in these cases indicates non-active areas of the lens.

of 15 arcsec. Such simulations of a hypothetical double Laue diffraction lens show that the PSF is way smaller and cleaner than the one obtained by a single diffraction lens. The simulated Half Power Diameter (HPD) for the double diffraction lens, in fact it is approximately half of the HPD for a single diffraction lens made by the same type of crystals (Fig. 4.6). The sim-

4.2. DOUBLE BRAGG'S DIFFRACTION IN LAUE CONFIGURATION 63

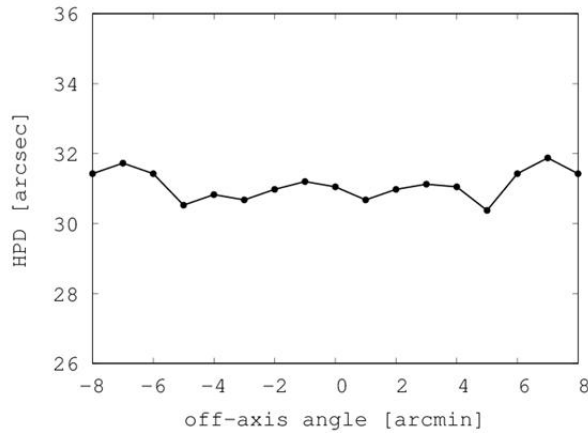


Figure 4.8: Simulated values of the HPD of a double diffraction Laue lens for some values of the off-axis angles.

ulation of the behaviour for off-axis sources also shows promising results. We can see that when the source is on-axis, all the coupled crystals on the ring are able to diffract the radiation selectively at different energies. On the other hand, when the source is off-axis, the number of crystal couples able to diffract is progressively reduced. The shape of the PSF, however, is not significantly changed (Fig. 4.7); in fact, the changes in the HPD appear to be very small, as shown in Fig. 4.8. This indicates that the effective area for off-axis sources becomes smaller, however the PSF is not significantly deformed, meaning that this new configuration is effective in removing the coma-like aberration which is present in the single diffraction case.

The double diffraction configuration, however, has two downsides: the reduction of the reflection efficiency and the reduction of the diffracting area of the crystals. The reduction of the efficiency comes from the fact that the beam undergoes two Laue diffractions, so the total efficiency is the product of the efficiency of the single crystals involved. In this configuration it is therefore crucial to use highly efficient crystal to avoid an excessive suppression of the beam.

The reduction of the diffracting area of the crystal instead comes from the fact that only a fraction of the total geometric area of the crystals is able to generate a double diffraction. This fraction corresponds to the intersection of the active area at a given energy on both crystals, so the total active area results in a thin region along the diagonal of the crystals (Fig. 4.9). This effect has been confirmed by simulations, which also showed that the thickness of the diagonal line depends on the quality of the coupling between the two crystals (Fig. 4.10). We can roughly estimate the order of magnitude of the diffracting area of the coupling in the case of square crys-

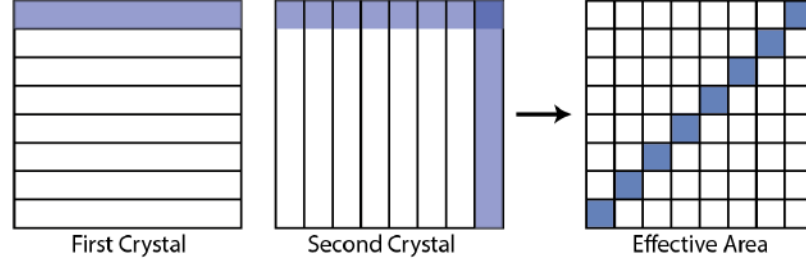


Figure 4.9: Visual representation of the effective area of two coupled crystals. The total active area of the couple of crystals is given by the intersection of the active areas at a given energy on the two crystals. The total effective area is a thin, diagonal region.

tals as the product between the diagonal of the crystal d and the width of one strip, which we can assume to be approximately the width of the beam after one diffraction, i.e. the size of the PSF of the first crystal. If we measure the PSF with its FWHM, we can write:

$$A_{couple} \sim d \cdot \text{FWHM} \quad (4.12)$$

The exact size of the PSF depends on the type of crystal used, however from previous measurements (Virgilli et al. 2015), we know that in the case of the crystals available in our laboratory (Perfect Si or mosaic GaAs crystals) the size of the PSF is slightly more than 1 mm. For a square crystal with a 10 mm side, we can then write $\text{FWHM} \sim l/10$, where l is the crystal length. So we then obtain:

$$A_{couple} \sim \sqrt{2} l \cdot \frac{l}{10} \sim l^2 \frac{\sqrt{2}}{10} \sim 0.14 A_{geom} \quad (4.13)$$

So we expect the active area of the coupling to be at least between one or two order of magnitude smaller than the geometrical area of a single crystal.

However, we expect that those disadvantages are balanced by a remarkable improvement of the quality of the PSF and a significant reduction of the coma-like distortion with respect to the case of a single diffraction. A double-diffraction lens can be a way to obtain a wider field imaging up to energy of about 1 MeV, when compared to single diffraction Laue lenses.

Based on these first interesting results, we decided to verify at the LARIX lab the feasibility of a coupling of two crystals, by obtaining some preliminary measurements of the off-axis performance of this first double Laue diffraction system.

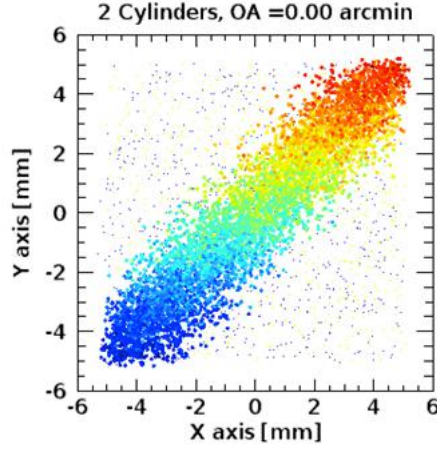


Figure 4.10: Ray-tracing simulation of the active area for two coupled bent mosaic crystals. The photons are color-coded on the base of their energy, from lower (red, 158 keV) to higher energies (blue, 162 keV). The two crystals have a cross-section of $10 \times 10 \text{ mm}^2$ and a mosaicity of 15 arcsec.

4.2.1 Experimental set-up and verification

We decided to use two square Gallium Arsenide (GaAs) crystals, which were cut from the same same ingot, with a cross section of $10 \times 10 \text{ mm}^2$ and a thickness of 2 mm, bent with a technique based on surface lapping (Ferrari et al. 2012, Buffagni et al. 2013). The two crystals have a measured curvature radius of respectively $(38.6 \pm 2.4) \text{ m}$ and $(38.9 \pm 2.9) \text{ m}$. GaAs is a mosaic crystal, so its internal structure is different from the perfect crystals described in the previous Chapters, nonetheless it has the same focusing properties of perfect curved curved crystals and can be used for our needs.

The measured mosaicity of the crystals is of $13 \pm 2 \text{ arcsec}$. We used the (220) diffracting planes, which are cut parallel to the edges of the crystal. The efficiency of GaAs (220) peaks at above 160 keV, so we decided to orient the crystals to diffract near this energy. The detectors used are a gamma-ray imaging detector with a sensitive area of $20 \times 20 \text{ cm}^2$ and a spatial resolution of $200 \mu\text{m}$ and an HPGe detector with a diameter of 2.5 cm and an energy resolution of $0.5 \text{ keV @ } 122 \text{ keV}$. To correctly place the detectors, we must take in account the divergence of the X-ray beam. When divergence is present, it has been shown (Virgilli et al. 2015) that the curvature radius of the crystals, the distance between the source and the crystals and the focal length are related by the formula valid at small Bragg's angles:

$$\frac{1}{F_D} = \frac{1}{D} + \frac{2}{R_C} \quad (4.14)$$



Figure 4.11: Experimental configuration of the two coupled crystals. *Left photo*: side view of the crystals. The quartz frame on which one of the two crystals is glued is the sheet on the left side, while on the right side one can see the rotatable sample holder with the adjustable crystal. *Center photo*: front view of the coupled crystals. *Right photo*: the imager detector and the spectrometer used in our experiment.

In our case, $D = (24.60 \pm 0.02)$ m, which yields a focal length of 11.39 m, so the detector was then placed at a distance of (11.4 ± 0.1) m from the crystals. We fixed one of the two crystals to a quartz frame with an UV-gel, while the other is held in position by a rotating sample holder, which can be positioned by a 6-axis hexapod system. The hexapod allows us to move the sample holder with orientation uncertainties of 1 arcsec and translation uncertainties of $1 \mu\text{m}$, while the sample holder allows the crystal to be positioned with an uncertainty of 1° . The adjustable crystal was the first crystal hit by the beam, while the fixed crystal was the second. The next step was to decide how to position the two crystals. Due to the effect of the second diffraction, the beam is sent to a direction of above 45° with respect to the direction of the single diffraction case, while the acquisition system at the LARIX-Tunnel facility is optimized for the single diffraction case, which makes such a high bending angle hard to detect. So we decided to position the first crystal to an angle of -45° and to fix the second one to an angle of $+45^\circ$, in this way the diffraction planes of the two crystals were at an angle of 90° between each and we were still able to easily intercept the beam with our detectors. To couple the two crystals, first we positioned the fixed crystal. We positioned the crystal at the Bragg's angle for 160 keV, which for GaAs(220) is 1.1° , then we rotated the crystal by an angle of $+45^\circ$ around the direction of the beam. In this way the image produced by this first crystal was rotated on the focal plane by $+45^\circ$ around the axis of the lens. We checked the correct positioning of the crystal both with the imager detector and with the spectrometer. Then the crystal has been glued to the quartz frame in this position.

The adjustable crystal was then mounted on the rotating frame, posi-

4.2. DOUBLE BRAGG'S DIFFRACTION IN LAUE CONFIGURATION 67

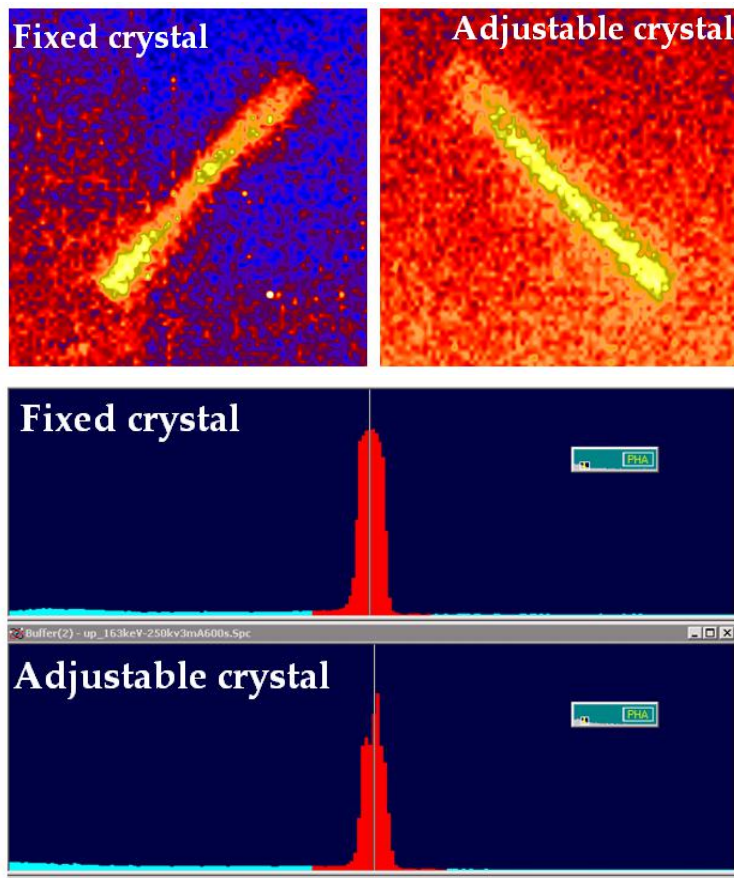


Figure 4.12: *Top:* Diffracted images produced by the two crystals separately. The fixed crystal is oriented to an angle of $+45^\circ$, while the other is oriented to an angle of -45° . The observation time is 300 sec for both images. *Bottom:* Measured spectra of the beams diffracted by the two crystals separately. The signal by the fixed crystal is centered around 163.6 keV, with FWHM of 7.0 keV. The signal of the adjustable crystal is centered around 163.3 keV and its FWHM is about 5.8 keV.

tioned at the Bragg's angle and then rotated by an angle of -45° . We moved the frame on which we mounted the previous crystal and, as we did before, we checked for the correct positioning of this crystal.

The diffracted images produced by the single crystals and their corresponding spectra are shown in Fig. 4.12. The experimental configuration of the two crystals is shown in Fig. 4.11. The fixed crystal was then moved so that the two crystals were effectively overlapped (4.11, central photo). After this operation, we were able to detect the double diffracted in the expected position, both with the imaging detector and with the spectrometer (Fig. 4.13). The image is significantly fainter than those produced by each

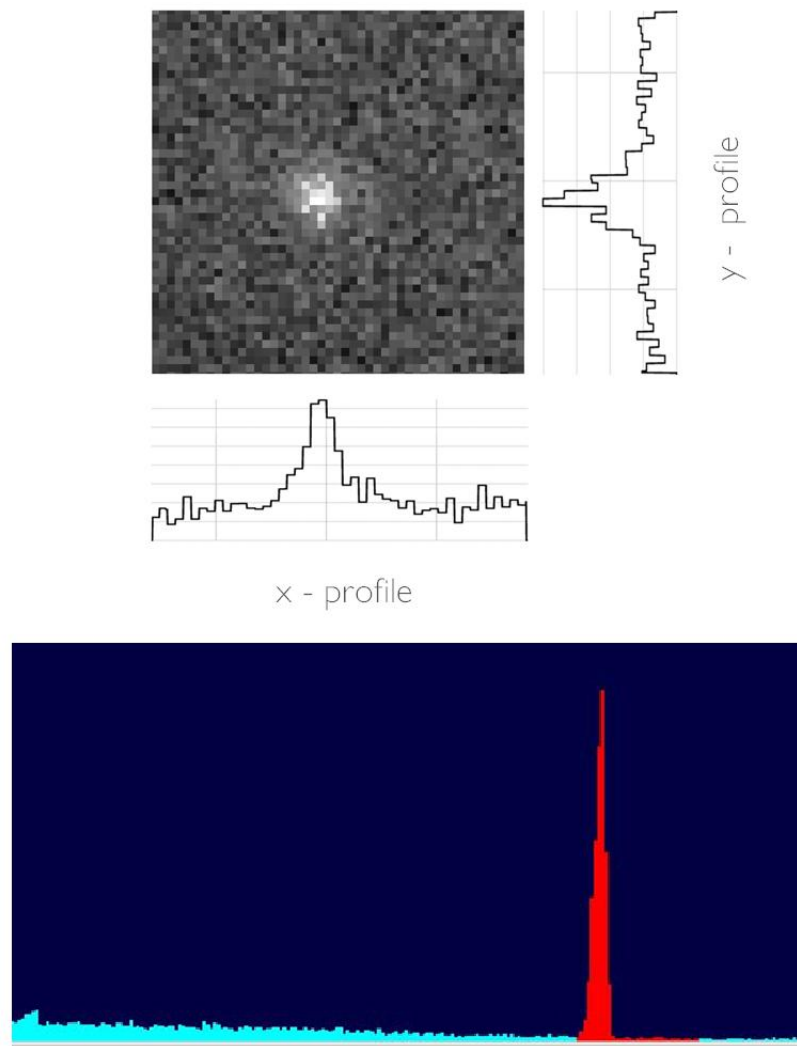


Figure 4.13: *Top*: Diffracted image produced by the two overlapping crystals. The integration time is 3000 sec. *Bottom*: the diffracted beam detected by the HPGe spectrometer. The signal is centered around 163.5 keV with a FWHM ≈ 3 keV.

crystal separately, so longer observation time are generally needed, however the signal has been clearly detected on both instruments. The FWHM of the x-profile of the diffracted beam is 1.0 mm, which corresponds to 10.3 arcsec, while the y-profile has a FWHM of 1.4 mm, which corresponds to 14.4 arcsec. Both measurements are comparable with the mosaicity of the crystals.

We then moved the source to obtain some preliminary measurements of the off-axis performances of the coupled crystals. Due to the low inten-

4.2. DOUBLE BRAGG'S DIFFRACTION IN LAUE CONFIGURATION 69

Off-axis [amin]	Obs. Time [s]	Energy [keV]	Count Rate
-5	300	150 ± 3	4.6 ± 0.1
-1	300	157 ± 4	5.8 ± 0.2
0	300	158 ± 4	7.6 ± 0.2
1	300	160 ± 4	7.0 ± 0.2
5	300	168 ± 5	7 ± 0.2
10	300	179 ± 4	1.6 ± 0.1

Table 4.1: Results of the off-axis performances test for two coupled crystals. The "Energy" column show the spectrum's centroid of the diffracted beam.

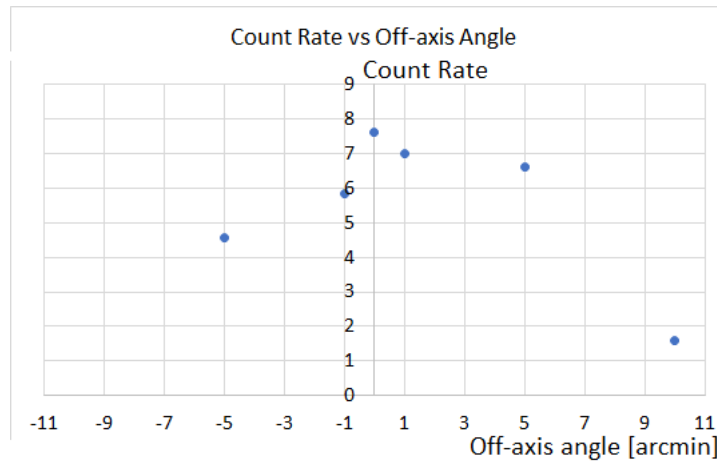


Figure 4.14: Plot of the count rate of the double diffracted beam for various off-axis angle of the source.

sity of the beam, the spectrometer is more suitable in this case, since long exposure times are required to obtain an image with a good S/N ratio. We adjusted the beam from the on-axis source on the center of the spectrometer window, then we started moving the source at increasing off-axis angles. Since the entrance window of the spectrometer is very small, we expect a fast drop in the count rate once the image becomes so deformed or shifted that part of the diffracted signal exits from the window. This first test was performed by moving the source along the vertical direction. The results are shown in Tab. 4.1 and Fig. 4.14.

This first test indicates that the count rate drops for an off-axis angle of 10 arcmin, however more data and further experimental activity will be needed to fully characterize the double diffracted beams at varying off-axis angles. However, these first tests have successfully verified the feasibility of the crystal coupling technique and have shown a significant improvement of the image quality.

4.2.2 Prospects for hard X-ray imaging with reduced off-axis aberrations

The experiments described above are the first demonstration that it is possible to significantly squeeze the source PSF thanks to double diffraction, thus enabling new techniques to obtain direct images in hard X-rays/soft γ -ray regime, in principle up to 1 MeV. This potentially opens a whole new field of applications for instruments based on Laue diffraction. For example, a much improved focusing technique can be extended to the field of medical X-ray imaging, crystallography and microscopy. The measured size of the PSF of the coupled crystals is of the order of 10 arcsec on both sides, which means that the coupling of the crystals is effective in focusing the radiation beam on both dimensions.

Due to the two consecutive diffractions, a significant reduction of the effective area is expected with respect to a single diffraction Laue lens. This reduction also affects the sensitivity of the instrument for on-axis source, which is however partially balanced by a sharp PSF, also for off-axis sources. The reduction of the on-axis effective area suggests that this technique is more suitable for sources with a high photon flux, which can be the case of sources used in industrial or medical context or bright astrophysical sources, such as GRB explosions in their first phase. The reduction of the coma aberration is a crucial aspect of this configuration, since it opens the possibilities to develop focusing instruments with a wider field-of-view, thus overcoming the known limitation of regular Laue lenses. The behaviour in the case of off-axis sources, however, needs to be experimentally validated. Clearly, an intense experimental activity is needed to fully assess the potential of this new Laue configuration. Specifically, we need to develop repeatable practical techniques to hold and fine tune the two crystals at once. In addition, we need to explore ways to permanently glue the two crystals together, thus obtaining a double diffracting tile. Alternative bonding techniques could be studied to create tiles with layered sandwiches of crystals. Nonetheless, the first results presented in this thesis have proved the feasibility of the double Laue diffraction scheme and indicated the multi-disciplinary potential of such a technique.

Conclusions

The aim of this thesis work was to advance the physical modeling and technological readiness to build a Laue lens at the core of the ASTENA (Advanced Surveyor of Transient Events and Nuclear Astrophysics) space mission concept. The work critically involved a number of experimental activities at the LARIX laboratory of the University of Ferrara. The following results have been obtained:

- **Estimate of the reflection efficiency for crystals of Silicon and Germanium.** We estimated for the first time the efficiency of bent, perfect crystals of Silicon and Germanium that will be used in the construction of ASTENA/Narrow Field Telescope (NFT). The method we used was described in Chapter 2 and allowed us to estimate the reflection efficiency as function of energy for the (111) and (333) planes of both types of crystals. This allowed an optimization of the distribution of the two types of crystals on the lens: Silicon will be used in the energy band [50 keV - 170 keV], where its efficiency prevails over Germanium, and Ge from 170 keV up to 600 keV. The estimated efficiency was used to evaluate the effective area of the ASTENA/NFT, thus providing the continuum and line sensitivity of the instrument. The sensitivity curves presented in the first Chapter confirm the vast increase of instrumental capabilities that will be brought by the ASTENA mission. The effective area has then been used to evaluate the response matrix of ASTENA/NFT, a key ingredient for conducting science feasibility studies by simulating observations. The efficiency model we developed can also be used to compute the efficiency of crystals made by different materials, with different curvature radius or different diffraction planes. This flexibility of this tool will facilitate further assessment studies of on ASTENA's performance, as well as of other future missions.
- **Upgrade of the Laue lens simulation software:** the *Laue Lens Library* software used for the simulation of Laue lenses has been expanded with the introduction of a Graphical User Interface, which makes the software more user-friendly, particularly for non expert users (i.e. other than the developers), who can now control the full

set of input parameters defining the physical components and geometrical configuration of the lens. Further functionalities were also added, such as the possibility to consider a distribution of parameters for the mosaicity/quasi-mosaicity of the crystals. This allows one to simulate lenses made by crystals with a fixed, uniform or Gaussian mosaicity distribution.

- **Study of the spectral performances of ASTENA/NFT:** Using the MEGALIB software, we computed the response matrix for the CdZTe detector used for the NFT, which is the first simulated response matrix for a Laue lens based instrument. Such a matrix, derived via Monte Carlo simulations, describes how the detector distributes a monochromatic signal across its spectral channels. The redistribution matrix of the detector is almost diagonal, meaning that it behaves approximately as an ideal detector for our energy band of interest (50 keV - 600 keV). This new development enables now to perform spectral simulations with the CZT/NFT detector for different types of astronomical sources. A first spectral simulation of NFT observations of the Crab Nebula has been presented.
- **Study of Laue lenses based on double Bragg's diffraction and first experimental validation:** In collaboration with the Brera Astronomical Observatory (INAF/OBA), we investigated the possibility to expand the concept of Laue lenses by considering a beam undergoing two consecutive diffractions through two crystals. The physical model and simulations we developed for this new configuration of a Laue lens illustrate that high-quality, hard X-/soft γ -ray images can be produced, with reduced coma aberrations and much improved off-axis performances when compared with the single diffraction lens. Specifically, this new study has shown that the double diffraction scheme improves the PSF over a broad energy band. We experimentally demonstrated that by coupling two crystals to produce a double diffracting beam, one can obtain the first direct image of a 160 keV beam. First preliminary tests of the off-axis performances of this new Laue configuration have also been performed.

This thesis work has contributed to show the potential of the ASTENA mission concept, which by combining a wide-field monitor with a narrow field focusing telescope could one day revolutionize astrophysics in the hard X-ray/soft γ -ray band, in a similar fashion to the great leap brought by grazing incidence reflecting optics to soft (<10 keV) X-ray astronomy in the seventies. Indeed, the computed expected sensitivity of NFT is ~ 1000 times higher than the today's available instrumentation, thus enabling narrow field observations with an unprecedented precision. Using the XSPEC software and the response matrix we built, we will be able to assess the fea-

4.2. DOUBLE BRAGG'S DIFFRACTION IN LAUE CONFIGURATION 73

sibility of a number of driving science cases, by simulating for example the continuum spectra of well-known sources or relevant emission lines, such as the 511 keV emission line observed in the galactic center, or the Nickel and Titanium nuclear lines in supernova remnants. This work paves the way to further developments of the ASTENA concept, specifically indicating some experimental activities necessary for the construction of the first prototype of Laue lens' petal at the LARIX laboratory. We plan to further expand the *Laue Lens Library* simulation software and to continue to study double diffraction configurations, by validating the off-axis model of coupled crystals, by studying the performances of different crystal types, and by exploring technical solutions to physically join the two crystals. In addition to the major advances that these developments may bring in the field of high energy astrophysics, it will also be interesting to explore multidisciplinary applications of new methods to focus high-energy radiation through Bragg's diffraction.

Bibliography

- B. P. Abbott, R. Abbott, T. D. Abbott, F. Acernese, K. Ackley, C. Adams, T. Adams, P. Addesso, R. X. Adhikari, V. B. Adya, and et al. Multimessenger observations of a binary neutron star merger. *The Astrophysical Journal*, 848(2):L12, Oct 2017. ISSN 2041-8213. doi: 10.3847/2041-8213/aa91c9. URL <http://dx.doi.org/10.3847/2041-8213/aa91c9>.
- I. Ahmad, J. P. Greene, E. F. Moore, S. Ghelberg, A. Ofan, M. Paul, and W. Kutschera. Improved measurement of the Ti44 half-life from a 14-year long study. *Physical Review C*, 74(6):065803, Dec. 2006. doi: 10.1103/PhysRevC.74.065803.
- M. Ajello, L. Baldini, G. Barbiellini, D. Bastieri, R. Bellazzini, E. Bissaldi, R. D. Blandford, R. Bonino, E. Bottacini, J. Bregeon, P. Bruel, R. Buehler, R. A. Cameron, R. Caputo, P. A. Caraveo, G. Chiaro, S. Ciprini, J. Cohen-Tanugi, D. Costantin, F. D'Ammando, F. de Palma, N. Di Lalla, M. Di Mauro, L. Di Venere, A. Domínguez, C. Favuzzi, A. Franckowiak, Y. Fukazawa, S. Funk, P. Fusco, F. Gargano, D. Gasparrini, N. Giglietto, F. Giordano, M. Giroletti, D. Green, I. A. Grenier, S. Guiriec, C. Holt, D. Horan, G. Jóhannesson, D. Kocevski, M. Kuss, G. La Mura, S. Larson, J. Li, F. Longo, F. Loparco, P. Lubrano, J. D. Magill, S. Maldera, A. Manfreda, M. N. Mazziotta, P. F. Michelson, T. Mizuno, M. E. Monzani, A. Morselli, M. Negro, E. Nuss, N. Omodei, M. Orienti, E. Orlando, V. S. Paliya, J. S. Perkins, M. Persic, M. Pesce-Rollins, F. Piron, G. Principe, J. L. Racusin, S. Rainò, R. Rando, M. Razzano, S. Razzaque, A. Reimer, O. Reimer, C. Sgrò, E. J. Siskind, G. Spandre, P. Spinelli, D. Tak, J. B. Thayer, D. F. Torres, G. Tosti, J. Valverde, M. Vogel, and K. Wood. Investigating the Nature of Late-time High-energy GRB Emission through Joint Fermi/Swift Observations. *The Astrophysical Journal*, 863(2):138, Aug. 2018. doi: 10.3847/1538-4357/aad000.
- G. Amelino-Camelia, J. Ellis, N. E. Mavromatos, D. V. Nanopoulos, and S. Sarkar. Tests of quantum gravity from observations of γ -ray bursts. *Nature*, 393(6687):763–765, Jun 1998. ISSN 1476-4687. doi: 10.1038/31647. URL <http://dx.doi.org/10.1038/31647>.

- N. Auricchio, E. Caroli, A. Basili, G. Benassi, C. Budtz Jørgensen, R. M. Curado da Silva, S. Del Sordo, I. Kuvvetli, L. Milano, F. Moscatelli, J. B. Stephen, M. Zanichelli, and A. Zappettini. Development status of a CZT spectrometer prototype with 3D spatial resolution for hard x-ray astronomy. In *High Energy, Optical, and Infrared Detectors for Astronomy V*, volume 8453 of *Society of Photo-Optical Instrumentation Engineers (SPIE) Conference Series*, page 84530S, July 2012. doi: 10.1117/12.928327.
- A. Authier. *Dynamical Theory of X-ray Diffraction*. IUCr OXFORD, 2003.
- K. W. Bannister, A. T. Deller, C. Phillips, J.-P. Macquart, J. X. Prochaska, N. Tejos, S. D. Ryder, E. M. Sadler, R. M. Shannon, S. Simha, and et al. A single fast radio burst localized to a massive galaxy at cosmological distance. *Science*, 365(6453):565–570, Jun 2019. ISSN 1095-9203. doi: 10.1126/science.aaw5903. URL <http://dx.doi.org/10.1126/science.aaw5903>.
- V. Bellucci, R. Camattari, V. Guidi, I. Neri, and N. Barrière. Self-standing bent silicon crystals for very high efficiency laue lens. *Experimental Astronomy*, 31:45–58, aug 2011. doi: 10.1007/s10686-011-9226-5.
- V. Bellucci, V. Guidi, R. Camattari, and I. Neri. Calculation of diffraction efficiency for curved crystals with arbitrary curvature radius. *Journal of Applied Crystallography*, 46(2):415–420, 2013. doi: 10.1107/S0021889813000162. URL <https://onlinelibrary.wiley.com/doi/abs/10.1107/S0021889813000162>.
- C. Boehm. The dark matter interpretation of the 511 keV line. *New Journal of Physics*, 11(10):105009, Oct. 2009. doi: 10.1088/1367-2630/11/10/105009.
- L. Bouchet, A. Strong, E. Jourdain, J. Roques, T. Porter, I. Moskalenko, R. Diehl, and E. Orlando. A complete all-sky survey with integral/spi: Sources census, hard x-ray diffuse emission and annihilation line. *The Extreme Sky: Sampling the Universe above 10 KeV*, 01 2009.
- E. Buffagni, E. Bonnini, A. Zappettini, G. Guadalupi, F. Rossi, and C. Ferrari. Crystal bending by surface damaging in mosaic gaas crystals for the laue project. *Proc SPIE*, 8861, 09 2013. doi: 10.1117/12.2024546.
- E. Churazov, R. Sunyaev, J. Isern, J. Knödseder, P. Jean, F. Lebrun, N. Chugai, S. Grebenev, E. Bravo, S. Sazonov, and M. Renaud. Cobalt-56 γ -ray emission lines from the type Ia supernova 2014J. *Nature*, 512(7515): 406–408, Aug. 2014. doi: 10.1038/nature13672.
- B. Cullity. *Elements of X-ray Diffraction*. Addison-Wesley series in metallurgy and materials. Addison-Wesley Publishing Company, 1978. ISBN 9780201011746. URL <https://books.google.it/books?id=WpxpAAAAMAAJ>.

- R. Diehl. Gamma rays from a supernova of type Ia: SN2014J. *Astronomische Nachrichten*, 336(5):464, June 2015. doi: 10.1002/asna.201512179.
- R. Diehl, T. Siegert, W. Hillebrandt, S. A. Grebenev, J. Greiner, M. Krause, M. Kromer, K. Maeda, F. Röpke, and S. Taubenberger. Early ^{56}Ni decay gamma rays from SN2014J suggest an unusual explosion. *Science*, 345(6201):1162–1165, Sept. 2014. doi: 10.1126/science.1254738.
- C. Ferrari, E. Buffagni, L. Marchini, and A. Zappettini. High-resolution x-ray characterization of mosaic crystals for hard x-ray astronomy. *Optical Engineering*, 51(4):046502-046502-5, Apr. 2012. doi: 10.1117/1.OE.51.4.046502.
- F. Frontera and P. V. Ballmoos. Laue gamma-ray lenses for space astrophysics: status and prospects. *astro-ph.IM*, 2011. doi: arXiv:1007.4308v3. URL [arXiv:1007.4308v3](http://arxiv.org/abs/1007.4308v3).
- F. Frontera, E. Virgili, C. Guidorzi, P. Rosati, R. Diehl, T. Siegert, C. Fryer, L. Amati, N. Auricchio, R. Campana, E. Caroli, F. Fuschino, C. Labant, M. Orlandini, E. Pian, J. Stephen, S. Del Sordo, C. Budtz-Jorgensen, I. Kuvvetli, S. Brandt, R. M. Curado de Silva, P. Laurent, E. Bozzo, P. Mazzali, and M. Della Valle. Understanding the origin of the positron annihilation line and the physics of the supernova explosions. 2019.
- J. P. U. Fynbo, J. Hjorth, D. Malesani, J. Sollerman, D. Watson, P. Jakobsson, J. Gorosabel, and A. O. Jaunsen. Gamma-ray burst host galaxies and the link to star-formation. *The Eleventh Marcel Grossmann Meeting*, Sep 2008. doi: 10.1142/9789812834300_0033. URL http://dx.doi.org/10.1142/9789812834300_0033.
- R. Giacconi. The high energy X-ray universe. *Proceedings of the National Academy of Science*, 107:7202–7207, Apr. 2010. doi: 10.1073/pnas.0913079107.
- R. Giacconi, H. Gursky, F. R. Paolini, and B. B. Rossi. Evidence for x Rays From Sources Outside the Solar System. *Physical Review Letters*, 9:439–443, Dec. 1962. doi: 10.1103/PhysRevLett.9.439.
- J. Gómez-Gomar, J. Isern, and P. Jean. Prospects for Type IA supernova explosion mechanism identification with gama-rays. *Monthly Notices of the Royal Astronomical Society*, 295:1–9, Mar. 1998. doi: 10.1046/j.1365-8711.1998.29511115.x.
- B. W. Grefenstette, F. A. Harrison, S. E. Boggs, S. P. Reynolds, C. L. Fryer, K. K. Madsen, D. R. Wik, A. Zoglauer, C. I. Ellinger, D. M. Alexander, H. An, D. Barret, F. E. Christensen, W. W. Craig, K. Forster, P. Giommi, C. J. Hailey, A. Hornstrup, V. M. Kaspi, T. Kitaguchi, J. E. Koglin, P. H.

- Mao, H. Miyasaka, K. Mori, M. Perri, M. J. Pivovarov, S. Puccetti, V. Rana, D. Stern, N. J. Westergaard, and W. W. Zhang. Asymmetries in core-collapse supernovae from maps of radioactive ^{44}Ti in Cassiopeia A. *Nature*, 506(7488):339–342, Feb. 2014. doi: 10.1038/nature12997.
- B. W. Grefenstette, C. L. Fryer, F. A. Harrison, S. E. Boggs, T. DeLaney, J. M. Laming, S. P. Reynolds, D. M. Alexander, D. Barret, F. E. Christensen, W. W. Craig, K. Forster, P. Giommi, C. J. Hailey, A. Hornstrup, T. Kitaguchi, J. E. Koglin, L. Lopez, P. H. Mao, K. K. Madsen, H. Miyasaka, K. Mori, M. Perri, M. J. Pivovarov, S. Puccetti, V. Rana, D. Stern, N. J. Westergaard, D. R. Wik, W. W. Zhang, and A. Zoglauer. The Distribution of Radioactive ^{44}Ti in Cassiopeia A. *The Astrophysical Journal*, 834(1):19, Jan. 2017. doi: 10.3847/1538-4357/834/1/19.
- C. Guidorzi, R. Margutti, D. Brout, D. Scolnic, W. Fong, K. D. Alexander, P. S. Cowperthwaite, J. Annis, E. Berger, P. K. Blanchard, R. Chornock, D. L. Coppejans, T. Eftekhari, J. A. Frieman, D. Huterer, M. Nicholl, M. Soares-Santos, G. Terreran, V. A. Villar, and P. K. G. Williams. Improved Constraints on H_0 from a Combined Analysis of Gravitational-wave and Electromagnetic Emission from GW170817. *The Astrophysical Journal Letters*, 851(2):L36, Dec. 2017. doi: 10.3847/2041-8213/aaa009.
- C. Guidorzi, F. Frontera, E. Virgili, P. Rosati, R. Diehl, T. Siebert, C. Fryer, L. Amati, N. Auricchio, R. Campana, E. Caroli, F. Fuschino, C. Labant, M. Orlandini, E. Pian, J. Stephen, S. Del Sordo, C. Budtz-Jorgensen, I. Kuvvetli, S. Brandt, R. M. Curado de Silva, P. Laurent, E. Bozzo, P. Mazzali, and M. Della Valle. Deeper & broader: future observations in the x-/gamma-ray band of known and unknown explosive transients. 2019.
- F. A. Harrison, W. W. Craig, F. E. Christensen, C. J. Hailey, W. W. Zhang, and et al. The Nuclear Spectroscopic Telescope Array (NuSTAR) high-energy X-ray mission. *The Astrophysical Journal*, 2013.
- I. Johnson, W. N., J. Harnden, F. R., and R. C. Haymes. The Spectrum of Low-Energy Gamma Radiation from the Galactic-Center Region. *The Astrophysical Journal*, 172:L1, Feb. 1972. doi: 10.1086/180878.
- S. Keitel, C. Malgrange, T. Niemöller, and J. Schneider. Diffraction of 100 to 200 keV x-rays from an Si1-xGeX gradient crystal: Comparison with results from dynamical theory. *Acta crystallographica. Section A, Foundations of crystallography*, 55:855–863, 09 1999. doi: 10.1107/S010876739900313X.
- P. Kirkpatrick and A. V. Baez. Formation of optical images by x-rays. *J. Opt. Soc. Am.*, 38(9):766–774, Sep 1948. doi: 10.1364/JOSA.38.000766. URL <http://www.osapublishing.org/abstract.cfm?URI=josa-38-9-766>.

- P. Kumar and B. Zhang. The physics of gamma-ray bursts & relativistic jets. *Physics Reports*, 561:1–109, Feb 2015. ISSN 0370-1573. doi: 10.1016/j.physrep.2014.09.008. URL <http://dx.doi.org/10.1016/j.physrep.2014.09.008>.
- E. Kuulkers, P. R. den Hartog, J. J. M. in't Zand, F. W. M. Verbunt, W. E. Harris, and M. Cocchi. Photospheric radius expansion X-ray bursts as standard candles. *Astronomy and Astrophysics*, 399:663–680, Feb. 2003. doi: 10.1051/0004-6361:20021781.
- I. Kuvvetli. *Development of CdZnTe detector systems for space applications*. PhD thesis, 2003.
- I. Kuvvetli, C. Budtz-Jørgensen, A. Zappettini, N. Zambelli, G. Benassi, E. Kalemci, E. Caroli, J. B. Stephen, and N. Auricchio. A 3D CZT high resolution detector for x- and gamma-ray astronomy. In *High Energy, Optical, and Infrared Detectors for Astronomy VI*, volume 9154 of *Society of Photo-Optical Instrumentation Engineers (SPIE) Conference Series*, page 91540X, July 2014. doi: 10.1117/12.2055119.
- M. Leventhal, C. J. MacCallum, and P. D. Stang. Detection of 511 keV positron annihilation radiation from the galactic center direction. *The Astrophysical Journal Letters*, 225:L11–L14, Oct. 1978. doi: 10.1086/182782.
- E. Liang, B. Zhang, F. Virgili, and Z. G. Dai. Low-luminosity gamma-ray bursts as a unique population: Luminosity function, local rate, and beaming factor. *The Astrophysical Journal*, 662(2):1111–1118, Jun 2007. ISSN 1538-4357. doi: 10.1086/517959. URL <http://dx.doi.org/10.1086/517959>.
- C. Malgrange. X-ray propagation in distorted crystals: From dynamical to kinematical theory. *Crystal Research and Technology*, 37, 07 2002. doi: 10.1002/1521-4079(200207)37:7<654::AID-CRAT654>3.0.CO;2-E.
- M. L. McConnell. High energy polarimetry of prompt grb emission. *New Astronomy Reviews*, 76:1–21, Feb 2017. ISSN 1387-6473. doi: 10.1016/j.newar.2016.11.001. URL <http://dx.doi.org/10.1016/j.newar.2016.11.001>.
- R. Morrison and D. McCammon. Interstellar photoelectric absorption cross sections, 0.03-10 keV. *The Astrophysical Journal*, 270:119–122, July 1983. doi: 10.1086/161102.
- W. R. Purcell, D. A. Grabelsky, M. P. Ulmer, W. N. Johnson, R. L. Kinzer, J. D. Kurfess, M. S. Strickman, and G. V. Jung. OSSE observations of Galactic 511 keV annihilation radiation. In M. Friedlander, N. Gehrels, and D. J. Macomb, editors, *American Institute of Physics Conference Series*,

volume 280 of *American Institute of Physics Conference Series*, pages 107–118, Jan. 1993. doi: 10.1063/1.44177.

- M. Pursiainen, M. Childress, M. Smith, S. Prajs, M. Sullivan, T. M. Davis, R. J. Foley, J. Asorey, J. Calcino, D. Carollo, C. Curtin, C. B. D’Andrea, K. Glazebrook, C. Gutierrez, S. R. Hinton, J. K. Hoormann, C. Inserra, R. Kessler, A. King, K. Kuehn, G. F. Lewis, C. Lidman, E. Macaulay, A. Möller, R. C. Nichol, M. Sako, N. E. Sommer, E. Swann, B. E. Tucker, S. A. Uddin, P. Wiseman, B. Zhang, T. M. C. Abbott, F. B. Abdalla, S. Allam, J. Annis, S. Avila, D. Brooks, E. Buckley-Geer, D. L. Burke, A. Carnero Rosell, M. Carrasco Kind, J. Carretero, F. J. Castander, C. E. Cunha, C. Davis, J. De Vicente, H. T. Diehl, P. Doel, T. F. Eifler, B. Flaugher, P. Fosalba, J. Frieman, J. García-Bellido, D. Gruen, R. A. Gruendl, G. Gutierrez, W. G. Hartley, D. L. Hollowood, K. Honscheid, D. J. James, T. Jeltema, N. Kuropatkin, T. S. Li, M. Lima, M. A. G. Maia, P. Martini, F. Menanteau, R. L. C. Ogando, A. A. Plazas, A. Roodman, E. Sanchez, V. Scarpine, R. Schindler, R. C. Smith, M. Soares-Santos, F. Sobreira, E. Suchyta, M. E. C. Swanson, G. Tarle, D. L. Tucker, A. R. Walker, and DES Collaboration. Rapidly evolving transients in the Dark Energy Survey. *Monthly Notices of the Royal Astronomical Society*, 481(1):894–917, Nov. 2018. doi: 10.1093/mnras/sty2309.
- V. Ravi, M. Catha, L. D’Addario, S. G. Djorgovski, G. Hallinan, R. Hobbs, J. Kocz, S. R. Kulkarni, J. Shi, H. K. Vedantham, and et al. A fast radio burst localized to a massive galaxy. *Nature*, 572(7769):352–354, Jul 2019. ISSN 1476-4687. doi: 10.1038/s41586-019-1389-7. URL <http://dx.doi.org/10.1038/s41586-019-1389-7>.
- T. Siebert, R. Diehl, A. C. Vincent, F. Guglielmetti, M. G. H. Krause, and C. Boehm. Search for 511 keV emission in satellite galaxies of the Milky Way with INTEGRAL/SPI. *Astronomy and Astrophysics*, 595:A25, Oct. 2016. doi: 10.1051/0004-6361/201629136.
- G. Skinner, R. Diehl, X.-L. Zhang, L. Bouchet, and P. Jean. The galactic distribution of the 511 keV e^+/e^- annihilation radiation. page 054, 03 2015. doi: 10.22323/1.228.0054.
- B. J. Teegarden, T. L. Cline, N. Gehrels, D. Palmer, R. Ramaty, H. Seifert, K. H. Hurley, D. A. Landis, N. W. Madden, D. Malone, R. Pehl, and A. Owens. TGRS Observation of the Galactic Center Annihilation Line. *The Astrophysical Journal Letters*, 463:L75, June 1996. doi: 10.1086/310061.
- S. P. Tendulkar, C. G. Bassa, J. M. Cordes, G. C. Bower, C. J. Law, S. Chatterjee, E. A. K. Adams, S. Bogdanov, S. Burke-Spolaor, B. J. Butler, P. Demorest, J. W. T. Hessels, V. M. Kaspi, T. J. W. Lazio, N. Maddox, B. Marcote, M. A. McLaughlin, Z. Paragi, S. M. Ransom, P. Scholz, A. Seymour, L. G.

- Spitler, H. J. van Langevelde, and R. S. Wharton. The Host Galaxy and Redshift of the Repeating Fast Radio Burst FRB 121102. *The Astrophysical Journal Letters*, 834(2):L7, Jan. 2017. doi: 10.3847/2041-8213/834/2/L7.
- G. Vedrenne, J. P. Roques, V. Schönfelder, P. Mandrou, G. G. Lichti, A. von Kienlin, B. Cordier, S. Schanne, J. Knödlseeder, G. Skinner, P. Jean, F. Sanchez, P. Caraveo, B. Teegarden, P. von Ballmoos, L. Bouchet, P. Paul, J. Matteson, S. Boggs, C. Wunderer, P. Leleux, G. Weidenspointner, P. Durouchoux, R. Diehl, A. Strong, M. Cassé, M. A. Clair, and Y. André. SPI: The spectrometer aboard INTEGRAL. *Astronomy and Astrophysics*, 411:L63–L70, Nov. 2003. doi: 10.1051/0004-6361:20031482.
- E. Virgilli, F. Frontera, P. Rosati, V. Liccardo, S. Squerzanti, V. Carassiti, E. Caroli, N. Auricchio, and J. B. Stephen. Hard x-ray broad band Laue lenses (80–600 keV): building methods and performances. In *Society of Photo-Optical Instrumentation Engineers (SPIE) Conference Series*, volume 9603 of *Society of Photo-Optical Instrumentation Engineers (SPIE) Conference Series*, page 960308, Sept. 2015. doi: 10.1117/12.2190335.
- E. Virgilli, V. Valsan, F. Frontera, E. Caroli, V. Liccardo, and J. B. Stephen. Expected performances of a Laue lens made with bent crystals. *Journal of Astronomical Telescopes, Instruments, and Systems*, 3:044001, Oct. 2017. doi: 10.1117/1.JATIS.3.4.044001.
- G. Weidenspointner, G. Skinner, P. Jean, J. Knödlseeder, P. von Ballmoos, and et al. An asymmetric distribution of positrons in the galactic disk revealed by γ -rays. *Nature*, 451:159–162, Jan. 2008.
- H. Wolter. Verallgemeinerte Schwarzschildsche Spiegelsysteme streifender Reflexion als Optiken für Röntgenstrahlen. *Annalen der Physik*, 445(4): 286–295, Jan. 1952. doi: 10.1002/andp.19524450410.
- W. H. Zachariasen. *Theory of X-ray Diffraction in Crystals*. Wiley, 1945.
- S.-N. Zhang, M. Kole, T.-W. Bao, T. Batsch, T. Bernasconi, F. Cadoux, J.-Y. Chai, Z.-G. Dai, Y.-W. Dong, N. Gauvin, W. Hajdas, M.-X. Lan, H.-C. Li, L. Li, Z.-H. Li, J.-T. Liu, X. Liu, R. Marcinkowski, N. Produit, S. Orsi, M. Pohl, D. Rybka, H.-L. Shi, L.-M. Song, J.-C. Sun, J. Szabelski, T. Tymieniecka, R.-J. Wang, Y.-H. Wang, X. Wen, B.-B. Wu, X. Wu, X.-F. Wu, H.-L. Xiao, S.-L. Xiong, L.-Y. Zhang, L. Zhang, X.-F. Zhang, Y.-J. Zhang, and A. Zwolinska. Detailed polarization measurements of the prompt emission of five gamma-ray bursts. *Nature Astronomy*, 3:258–264, Jan. 2019. doi: 10.1038/s41550-018-0664-0.
- A. Zoglauer, R. Andritschke, and F. Schopper. MEGAlib The Medium Energy Gamma-ray Astronomy Library. *New Astronomy Review*, 50(7-8): 629–632, Oct. 2006. doi: 10.1016/j.newar.2006.06.049.